U.PORTO
FLUP FACULDADE DE LETRAS
UNIVERSIDADE DO PORTO

FLUP-MSIGOT-2023/2024-2S
MASTER'S DEGREE IN GEOGRAPHIC INFORMATION SYSTEMS AND SPATIAL PLANNING
DEPARTMENT OF GEOGRAPHY

Comparative Study of Random Forest and SVM for Land Cover Classification and Post-Wildfire Change Detection

Tan Yan Cheng

M

2024

Supervisor

Dra. Ana Cláudia Teodoro, Associate Professor with Habilitation, Department of Geoscience, Environment and Land Planning, Faculty of Science, University of Porto

Co-supervisor

Dr. José Augusto Alves Teixeira, MSc, PhD, Assistant Professor, Director of Master's Degree in Geographic Information Systems and Spatial Planning, Department of Geography, Faculty of Arts, University of Porto

Tan Yan Cheng

Comparative Study of Random Forest and SVM for Land Cover Classification and Post-Wildfire Change Detection

Dissertation carried out within the scope of the master's degree in Geographic Information Systems and Spatial Planning, supervised by Professor Ana Cláudia Teodoro and by Professor José Augusto Alves Teixeira.

Faculty of Arts of the University of Porto

June 26, 2024

To my family.

Declaration of honor

I declare that this dissertation titled "Comparative Study of Random Forest and SVM for Land Cover Classification and Post-Wildfire Change Detection" is my own work and has not been previously used in any other course or curricular unit, from this or another institution. References to other authors (statements, ideas, thoughts) scrupulously respect the rules of attribution and are duly indicated in the text and bibliographical references in accordance with the referencing rules. I am aware that the practice of plagiarism and self-plagiarism constitutes an academic offence.

Porto, 26.06.2024

Tan Yan Cheng

Acknowledgements

First and foremost, I would like to express my sincere gratitude to my supervisor, Dra. Ana Cláudia Teodoro, as well as my professors, Dr. José Augusto Alves Teixeira, Dr. António Alberto Teixeira Gomes, and Dr. Miguel Marinho Saraiva, for their continuous guidance, assistance, and encouragement throughout my master´s program. Their mentorship has been an invaluable asset to my academic and professional development.

I want to extend a special thank you to the friends I have made in Europe, who have been strong pillars and part of the wonderful memories of my life journey. I am especially grateful to Fernanda, Yibo, Xiwen, Filipa, Alex, David, Stefan, and Ashwin for their unwavering friendship and support.

Lastly, I would like to dedicate this research to my beloved family and friends in Malaysia, whose constant support and love have been a source of strength in my life.

Abstract

Land use land cover (LULC) map is extensively employed by different entities/stakeholders for research, analysis, planning, and monitoring purposes. However, the LULC maps provided by the National Geographic Information System (SNIG) in Portugal, which are updated every three to five years for the Land Use and Occupation Map (COS) and annually for the Conjunctural Land Occupation Map (COSc), are inadequate for continuous assessment and regular scrutiny on the land cover change. Machine learning (ML) for remote sensing (RS) has been explored by researchers since the late 1990s and has proven effective in image classification, object detection, and semantic segmentation since the 2010s. Today, machine learning and remote sensing integration has been widely applied in environmental monitoring, urban planning, disaster management, agriculture and more. Previous studies have shown that Random Forest (RF) and Support Vector Machine (SVM) consistently achieved high accuracy for land classification while recent studies found Extreme Gradient Boost (XGB) outperforming RF. In this research, the application of RF and SVM classifiers with Sentinel-2A imagery was evaluated to identify the most appropriate ML algorithms using Google Earth Engine (GEE) for land cover classification of a burned area in the Serra da Estrela Natural Park (PNSE). This was aimed to detect the land cover change, and closely observe the burned area and vegetation recovery after the 2022 wildfire. Land cover maps of pre-wildfire 2022, post-wildfire 2022, and summer 2023 were generated using object-based (OBIA) and pixel-based (PBIA) approaches and two classifiers: RF and SVM. The RF x OBIA model achieved the highest accuracy in all evaluation metrics for all events, while comparison with the Normalized Difference Vegetation Index (NDVI) map and COSc 2023 indicated that the SVM x PBIA map resembled the maps better. The best model for land cover classification of the study area was not conclusively determined as no field data is accessible for solid validation.

Key-words: Machine Learning, Land cover classification, Object-based image analysis, Pixel-based image analysis, Random Forest, Support Vector Machine

Contents

Index of Figures

Appendix A

Appendix B

Appendix D

Index of Tables

Appendix B

Appendix C

List of Abbreviations and Acronyms

ANN .... ARTIFICIAL NEURAL NETWORKS

COS .... LAND USE AND OCCUPATION MAP

COSC .... CONJUNCTURAL LAND OCCUPATION MAP

DEM .... DIGITAL ELEVATION MODEL

DGT .... GENERAL DIRECTORATE OF THE TERRITORY

DNBR .... DIFFERENCE NORMALIZED BURN RATIO

DTS .... DECISION TREES

EFFIS .... EUROPEAN FOREST FIRE INFORMATION SYSTEM

EPSG .... EUROPEAN PETROLEUM SURVEY GROUP

FCUP .... FACULTY OF SCIENCES

FN .... FALSE NEGATIVE

FP .... FALSE POSITIVE

GEE .... GOOGLE EARTH ENGINE

GEOBIA .... GEOGRAPHIC OBJECT-BASED IMAGE ANALYSIS

GIS .... GEOGRAPHIC INFORMATION SYSTEMS

GPS .... GLOBAL POSITIONING SYSTEM

ICNF .... INSTITUTE FOR NATURE CONSERVATION AND FORESTS

IDE .... INTEGRATED DEVELOPMENT ENVIRONMENT

K-NN .... K-NEAREST NEIGHBOURS

LUCAS .... LAND USE-LAND COVER AREA FRAME SURVEY

LIDAR .... LIGHT DETECTION AND RANGING

LULC .... LAND USE LAND COVER

ML .... MACHINE LEARNING

MLC .... MEDITERRANEAN LOCAL CONDITIONS

NDVI .... NORMALIZED DIFFERENCE VEGETATION INDEX

NBR .... NORMALIZED BURN RATIO

OA .... OVERALL ACCURACY

OBIA .... OBJECT-BASED IMAGE ANALYSIS

OSM .... OPEN STREET MAP

PBIA .... PIXEL-BASED IMAGE ANALYSIS

PNSE .... SERRA DA ESTRELA NATURAL PARK

QGIS .... QUANTUM GEOGRAPHIC INFORMATION SYSTEM

RBF .... RADIAL BASIS FUNCTION

RBR .... RELATIVIZED BURN RATIO

RF .... RANDOM FOREST

RGB .... RED GREEN BLUE

ROI .... REGION OF INTEREST

RS .... REMOTE SENSING

SCI .... SITE OF COMMUNITY INTEREST

SLI .... STREET-LEVEL IMAGERY

SMOS .... LAND OCCUPATION MONITORING SYSTEM

SNIC .... SIMPLE NON-ITERATIVE CLUSTERING

SNIG .... THE NATIONAL GEOGRAPHIC INFORMATION SYSTEM

SVM .... SUPPORT VECTOR MACHINE

TN .... TRUE NEGATIVE

TP .... TRUE POSITIVE

UAV .... UNMANNED AERIAL VEHICLES

USGS .... UNITED STATES GEOLOGICAL SURVEY

XGBOOST .... EXTREME GRADIENT BOOSTING

1. Introduction

1.1. Introduction

Post-wildfire land cover change affects the ecosystem dynamics, biodiversity system, and ecological processes [1, 2]. According to the European Commission, land cover indicates “the visible surface of land (e.g. crops, grass, water, broad-leaved, forest or built-up area)” [3]. Thus, land cover plays a key role in environmental conditions in multiple ways [4]. Several studies have proved that fire events change soil characteristics which increase runoff and erosion risk [5-7], plants diversity [8-10], habitat and species composition [11-13], water quality [14-16], climate [17-19], and carbon storage [20, 21]. Detecting the land cover change during a wildfire is critical, as it enables authorities to develop prompt disaster management strategies to prevent fatalities caused by landslides and flash floods following a wildfire [22]. Furthermore, periodic assessments scrutinizing burned area recovery and vegetation dynamics after a wildfire provide valuable information for land management and biodiversity recovery monitoring.

According to European Copernicus, Portugal is one of the countries which is most vulnerable to wildfire in the European Union [23]. On average, more than 200 forest fires happened in Portugal from 2013 to 2022 annually. Portugal experienced the worst drought in 2017 since 1931, which caused 408 wildfires and involved 563,532 hectares of burned area [24, 25]. The Serra da Estrela Natural Park (PNSE), the largest protected area in Portugal, experienced the largest fire since 1975 [26], which involved a burned area of 21,942 hectares in 2022 [27]. Sentinel-2A imagery was used to identify the burned area and define the study area in this research. The study area in this research focused on the major burned area in wildfire 2022. The fire spread beyond the PNSE to Estrela Geopark (Fig. 3). As a recognized Biogenetic Reserve and Geopark [28], the impacts of the large burned area post-wildfire 2022 in the PNSE are concerning. Close monitoring on post-wildfire burned area recovery and vegetation dynamic, to observe the ecosystem dynamics and plan for the disaster management is imperative.

In Portugal, the open data on land use and land cover (LULC) is publicly available from the National Geographic Information System (SNIG). The Land Use and Occupation Map (COS) was published between three to five years from 1995 to 2018. The Conjunctural Land Occupation Map (COSc), as complementary information to COS, has been published annually since 2018. Both COS and COSc are products of the Land Occupation Monitoring System (SMOS), an innovative initiative, designed and developed by the General Directorate of Territory (DGT). The COS serves as the primary reference cartography for planning, while the COSc demonstrates the land occupation not the land use in a specific year. COS is prepared in vector format at a scale of 1:25,000 with 44 classes of LULC with an exception where COS2018v2.0 has 83 classes of LULC. On the other hand, COSc is prepared in raster format with 10m pixels with 6, 9 and 13 classes at levels 1, 2 and 3, respectively, whereas subsequent maps have 15 classes at level 3 with improvement in the agriculture class. LULC maps are widely used by various stakeholders for research, analysis, planning, and monitoring purposes. However, continuous assessment and regular scrutiny on the land cover change are not achievable even with the annual update of COSc.

Integration of machine learning (ML) algorithms and remote sensing (RS) data has been explored by researchers since the late 1990s, and has proven effective in image classification, object detection, and semantic segmentation since the 2010s. Today, the integration of ML and RS has been widely applied to convert satellite imagery into valuable spatial data for environmental monitoring, urban planning, disaster management, agriculture and more. Previous studies proved that the integration of ML and RS techniques is more efficient in land cover classification and achieves higher accuracy [29, 30] compared to conventional methods [31]. Regardless, many studies have found Support Vector Machines (SVM) to outperform Random Forest (RF) [31-34]; RF has been proven to be one of the most efficient ML algorithms to be integrated with RS techniques for land cover classification [29, 30, 32].

1.2.Research Questions

This research aims to identify the most appropriate LULC approach and classifier for land cover classification to resolve the challenges faced for continuous assessment in the study area while serving as a reference for other forest regions that share similar characteristics. Analysis was conducted to answer the following research questions:

- Is the land cover map generated using RF and SVM classifiers adequate for monitoring burned area recovery after wildfire?
- Which method, Object-Based Image Analysis (OBIA) or Pixel-Based Image Analysis (PBIA), is more appropriate for land cover classification in the study area?

1.3.Objectives

As an alternative to the cost and time-consuming field data collection, the accuracy and reliability of land cover classification employing RS techniques with ML algorithms is crucial for researchers to conduct continuous assessment, regular scrutiny on the burned area recovery and vegetation dynamic monitoring, and temporal analysis at shorter interval in the study area. This study was conducted with several objectives:

- to identify the best model for land cover classification for the study area employing the integration of LULC classification with classifier on Google Earth Engine (GEE);
- to compare the effectiveness of two LULC classification methods: OBIA and PBIA;
- to compare the accuracy of RF and SVM algorithms for land cover classification, using GEE;
- to assess the accuracy of the land cover classification generated by different models with evaluation metrics, burned territories from Institute for Nature Conservation and Forests (ICNF), Normalized Difference Vegetation Index (NDVI) map, and COSc 2023 from SNIG;

- to detect the vegetation dynamic and burned area by computing NDVI and Normalized Burn Ratio (NBR) using Sentinel-2A imagery;
- to detect the land cover change between pre-wildfire 2022, post-wildfire 2022, and summer 2023, and observe the burned area recovery with the highest accuracy land cover maps.

1.4.Overview of the dissertation structure

This research is presented in 7 chapters demonstrating the content below:

- **Introduction**: This chapter introduces the context and importance of land cover classification and land cover change detection post-wildfire, the motivation to compare the ML algorithms to classify the land cover in the PNSE, the research questions and objectives of this research, and the structure overview;
- **Literature Review**: This chapter outlines the literature review of RS data and ML algorithms developments, as well as the application of the integration of RS and ML algorithms in land cover classification to observe the post-wildfire impacts;
- **Implementation**: This chapter briefs the main software used in this research: GEE and QGIS software;
- **Study area:** This chapter details the study area and importance of the PNSE.
- **Methodology**: This chapter explains the proposed approach to achieve the objectives of this research;
- **Results**: This chapter analyzes the land cover classification generated by different models, supported by chart, and table illustrations;
- **Discussion**: This chapter discusses the findings in relation to research questions, the accuracy of land cover maps classified by RF and SVM;
- Conclusions: This closing chapter concludes this research work and references for future work.

2. Literature Review

This chapter presents a comprehensive literature review covering the research topic. The literature review begins with an introduction to RS, the development of ML algorithms integrated with RS data/techniques for land cover classification and post-wildfire land cover change detection, and a comparative analysis of machine learning algorithms. Subsequently, the application of ML algorithms integrated with RS data/techniques for land cover classification and post-wildfire land cover change detection was discussed, highlighting their strengths and limitations.

2.1. Remote Sensing

In previous studies, Landsat imagery, Sentinel imagery, and aerial photographs are applied to analyze the land cover changes [33-35]. The advantages and capabilities of RS techniques, including large-scale coverage, frequent data, multispectral and hyperspectral capabilities, three-dimensional information, and cost-effectiveness, make them a common tool applied in various environmental studies.

Klobucar et al. studied that multispectral aerial imagery and Light Detection and Ranging (LIDAR) data provide comparable estimates of tree canopy as compared to ground base measurement, which is positive for land cover change detection [36]. In Pérez-Cabello et al.'s study, RS is the most practical technique to monitor changes over large areas and periods through image-processing techniques using either change detection or classification techniques [37]. In South Korea, RS techniques have been continuously used to detect the burnt areas and evaluate the recovery time point on the eastern coast after the major wildfire in April 2000, which was registered as the most serious wildfire in South Korean history [38].

Sentinel-2, as part of the European Commission's Copernicus Earth Observation (EO) program, was launched on 23 June 2015 and 7 March 2017 for Sentinel-2A and Sentinel-2B, respectively. The phase of both satellites on the same orbit 180 degrees from each other improves the revisit cycle from 10 days to 5 days. In addition, Sentinel-

2 has 13 spectral bands in high resolution from 10m to 60m [42], enabling the identification of key land features like vegetation, water bodies, and urban areas, initiating a paradigm shift in land cover classification. Sentinel-2 imagery was utilized to improve land cover maps in Iran [39], conduct land cover classification and change detection in Rusinga Island, Kenya [40], map smallholder agriculture in Antsirabe, Vakinankaratra region, Madagascar [41], assess wildfire damage in Australia [42], and map cropland in Continental Africa [43].

2.2. Integration of Machine Learning and Remote Sensing in Land Cover Classification and Post-Wildfire Land Cover Change Detection

Integration of ML algorithms and RS data in land cover classification was explored as early as in the 1990s. Huang and Jensen included Geographic Information Systems (GIS) data training, decision tree generation, and production rules to train the ML algorithm in building the automation system to classify the wetland in Par Pond on the Savannah River, South Carolina [31]. Stratified random sampling was applied to avoid undersampling. Training data were classified according to human experts and ground reference information into four classes: (a) wetland, (b) dead vegetation, (c) bare soil, and (d) water. A recursive strategy was used to generate the decision tree. The decision trees were then transformed into production rules to classify the dataset into one of four classes, where attributes with the minimum entropy were selected to classify the dataset. The resulting knowledge base was compared to the classification produced by conventional methods: (a) traditional supervised classification with spectral and GIS data, and (b) traditional unsupervised classification with only spectral data. This method, proposed by Huang and Jensen, tackled the labour-intensive issues encountered in conventional methods for data distribution [30] and provided valuable spatial information unattainable using the maximum-likelihood classification algorithm, which was widely used in remote sensing for image processing [44].

Lazzeri et al. employed several RS data/techniques, including PRISMA hyperspectral, multispectral Sentinel-2 data, and unmanned aerial vehicles (UAV), to assess the post-fire impacts on land cover in both Castanheira de Pêra Fire in the Leiria district, Portugal, and Vinchiana Fire in the Tuscany region, Italy [45]. The resulting Relativized Burn Ratio (RBR) index indicated that Sentinel-2 is effective for evaluation in large-scale burned areas, while providing valuable information on fire severity and vegetation recovery. Furthermore, integration of the PRISMA hyperspectral classification and Sentinel-2 data is optimal for fire severity classification even in situations where continuous data is not possible, as this method can distinguish the spectral signatures corresponding to different fire severity classes. Furthermore, the UAV proved to outperform traditional Global Positioning System (GPS) mapping in generating high-resolution mapping and categorizing burned areas.

Lasaponara et al. employed Sentinel-2 NDVI time series and GEE to identify the LULC changes in the central-southern part of the Italian peninsula from the year after the fire event to the present [46]. The linear regression method was selected using GEE to generate the NDVI trends and to understand the temporal changes, RF classification was then applied to detect the LULC changes. The result was split between training data and testing data in a 60:40 ratio and assessed with high-resolution images retrieved from Google Earth. This method achieved an overall accuracy (OA) higher than 0.86.

With the increasing popularity of Extreme Gradient Boosting (XGBoost), De Oliveira employed and compared XGB and RF, to enhance the LULC mapping of 2018 in Almada municipality, Portugal [47]. The research classified Sentinel-1 imagery, Sentinel-2 imagery, and derived products using both PBIA and OBIA approaches into five classes: (a) artificial territories, (b) agriculture, (c) other vegetation, (d) forests, and (e) bare and sparsely vegetated areas. Different combinations of satellite data and derived products were examined with XGBoost and RF classifiers. The result was compared with manual and semi-automatic collected ground truth data. De Oliveira concluded that land cover classification using both Sentinel-1 and Sentinel-2 imagery and textural features derived from Sentinel-2, with the PBIA approach classified with the XGBoost classifier indicated the best result for urban areas. This method achieved a kappa coefficient of 0.994 and had great accuracy in identifying the land cover classes, except for some limitations in distinguishing Agriculture and Other Vegetation. The inclusion of spectral indices in the data combination indicated a decrease in kappa coefficients in most of the classification results, while the inclusion of textural features increased the kappa coefficients slightly.

In a recent study, Martinez-Sanchez et al. utilized the Land Use-Land Cover Area Frame Survey (LUCAS) photographs and employed semantic segmentation and RF model to generate automatic land cover classification based on LUCAS in-situ landscape photos in Europe [48]. A computer vision methodology was developed to extract land cover information from the images obtained from LUCAS. In the study, 1120 images covering eight major land covers: (a) artificial land, (b) cropland, (c) woodland, (d) shrubland, (e) grassland, (f) bare soil and lichens, (g) water areas, and (h) wetlands, across the European Union, were selected. Deeplabv3+ [49, 50], a pre-trained semantic segmentation model, and ADE20k [51], a semantic segmentation dataset, were used to extract the land cover types in LUCAS images and classify the training dataset. The training dataset was then used as input features to train a RF model to classify the land cover classification of the image. Street-level imagery (SLI) land cover information validated and improved the result. This method produced a land cover classification with an F1 score of 89%; F1 score was improved to 93% if the wetland was excluded.

2.3.Comparative Analysis of Machine Learning Algorithms

In many studies conducted since then, the results were inconsistent in land cover classification accuracy using RF and SVM. Despite many studies that found SVM to outperform RF [52-55], RF has been proven to be one of the most efficient ML algorithms to be integrated with RS techniques for land cover classification.

Maxwell et al. reviewed the result generated by six mature ML classifiers integrated with RS: (a) SVM, (b) single decision trees (DTs), (c) RF, (d) boosted DTs, (e) artificial neural networks (ANN), and (f) k-nearest neighbours (k-NN), with two publicly available RS datasets: (a) the Indian Pines dataset, and (b) the Geographic Object-Based Image Analysis (GEOBIA) dataset[32]. Maxwell et al. suggested that RF is preferred when optimization is not possible, as the default parameter of RF achieves classification accuracy close to the result generated through optimization. ML algorithms were found to be more robust than parametric methods in dealing with complex feature spaces and useful when the feature selection is absent.

Rodriguez-Galiano et al. conducted a study in the south of Spain to assess the effectiveness of RF in land cover classification [30]. The study justified RF advantages of non-parametric nature, capability in variable importance determination, and high classification accuracy with the positive result of 92% OA and kappa coefficient of 0.92. Furthermore, Saini and Rawat compared four classifiers: (a) ANN, (b) SVM, (c) kNN, and (d) RF for LULC classification in the Nainital district situated in Uttarakhand, India, of which RF achieved the highest OA of 91.56% with a kappa coefficient of 0.899 [56]. Moreover, Aziz et al. applied ANN and RF for forest cover classification in the Abbottabad district of Pakistan [29]. The result produced by RF with the temporal layer stacked image of the Sentinel-2 satellite achieved exceptional performance with 99.79% training accuracy, 96.98% validation accuracy, and kappa coefficients of 0.996 and 0.954.

Lawrence and Moran conducted a study to compare the performance of six classifiers with consistent procedures, with 30 moderate-resolution and multispectral datasets: (a) C5.0, (b) classification tree analysis, (c) logistic model trees, (d) multivariate adaptive regression splines, (e) RF, and (f) SVM [57]. Despite the finding that RF achieved the highest average classification accuracy of 73.19%, Lawrence and Moran suggested the researchers evaluate multiple methods instead of using RF as the sole option for classification, as RF was not the classier that achieved the highest accuracy in all cases.

2.3.1.Random Forest (RF)

RF and SVM are both popular supervised learning algorithms for classification and regression. RF adopts an ensemble learning method (Fig. 1) formed by:

- **Bagging:** involves developing multiple models with random subsets of feature selection and training data.
- **Boosting:** each model iterates to fix the errors of previous models to achieve higher accuracy prediction.

- **Stacking:** a new model is then trained based on the output of the smaller models.

The final prediction is derived from the weighted outputs generated by the models ensembled in RF.

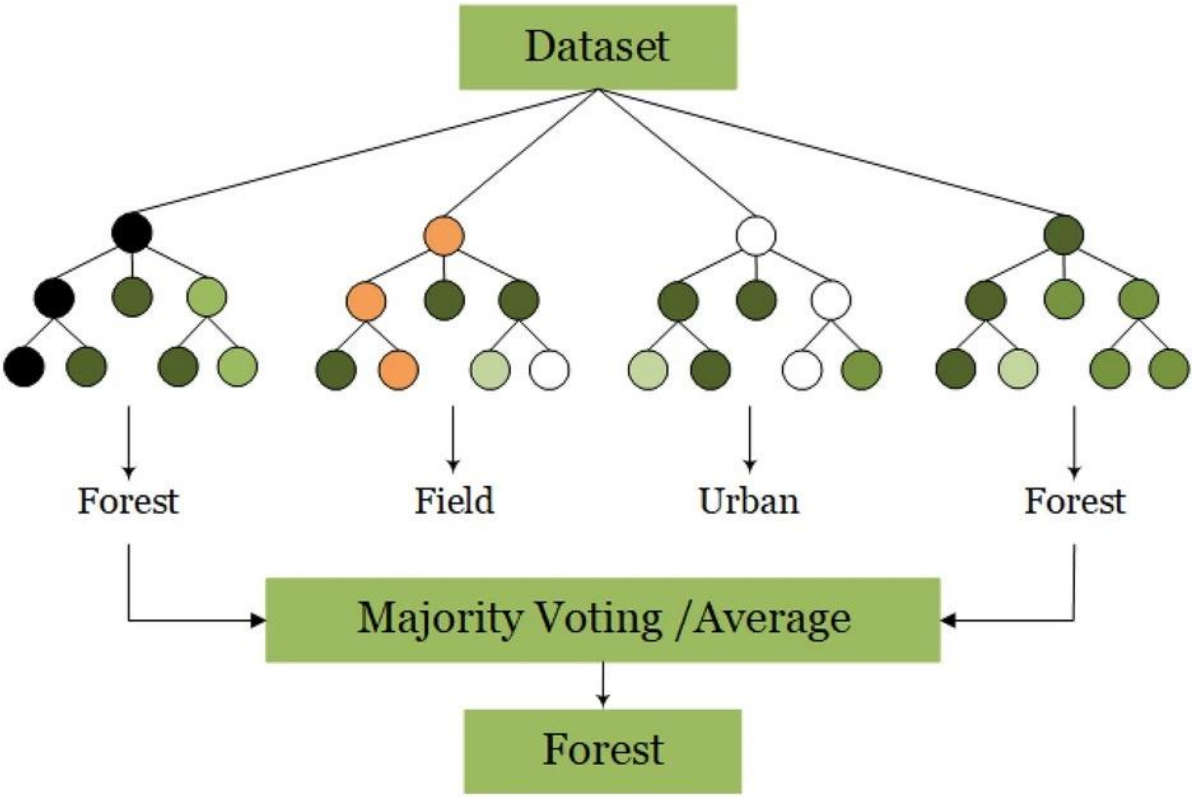

Figure 1. Random Forest illustration. Adapted from Aziz et al., 2024 [29].

Advantages

- As the final prediction is an average from several models, RF is more robust to data outliers and produces accurate results.
- RF tends to be better at generalizing to new data and less overfitting compared to other algorithms.
- RF handles high-dimensional data effectively without performance deterioration using ensemble learning methods.

Disadvantages

- Experimenting with the right hyperparameters is decisive in generating high accuracy RF prediction.
- RF cannot forecast values other than the feature range of the training data.

2.3.2.Support Vector Machine (SVM)

SVM uses kernel functions to find the best hyperplane (optimal line) based on the training data. SVM maximizes the margin between classes through a support vector. As shown in Fig. 2, the margin is the maximum distance between the closest pattern of two classes. There is no point included between the support vectors. The optimal hyperplane is determined after the margin is maximized; this is to define the best decision boundary for accurate predictions.

Advantages

- SVM can handle both linear and nonlinear tasks and is effective for training data with clear class separation.
- In the land cover classification context, SVM is robust to classify homogeneous and heterogeneous land cover classes [58].
- SVM can handle high-dimensional data and is robust to noise and outliers.
- SVM tends to handle skewed datasets better; this is an advantage where there is a big gap between the number of training points of different classes.
- Given that SVM employs only one subset of training points to generate the decision, it is memory efficient.

Disadvantages

- SVM is computationally expensive.
- It is not suitable for large dataset classification [59, 60].

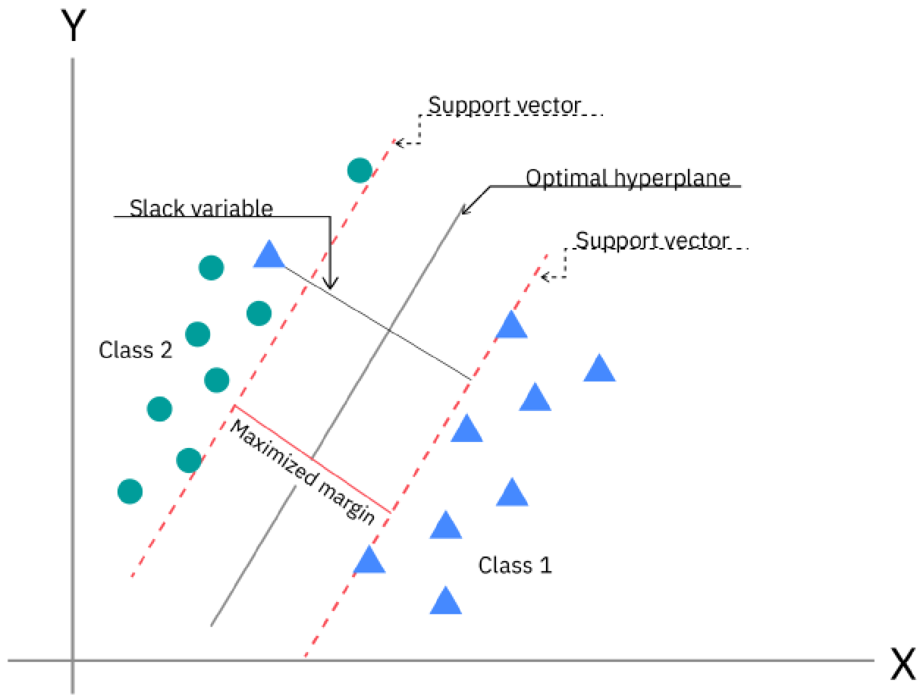

Figure 2. Support Vector Machines illustration. Adapted from IBM[1]

2.4. Object-Based Image Analysis (OBIA) vs Pixel-Based Image Analysis (PBIA)

OBIA and PBIA are two common approaches for LULC [47].

OBIA groups the neighbouring pixels with similar spectral properties and contextual information into meaningful objects. OBIA is useful for object identification in addition to pixel labelling. The quality of the object segmentation determines the final classification. Edge-based algorithms, region-based, and superpixel algorithms are common for OBIA segmentation [61].

Advantages

- OBIA utilizes spatial context, and makes it effective in homogeneous and heterogeneous landscapes.

[1] https://www.ibm.com/topics/support-vector-machine

- OBIA combines multiple features for better differentiation in classification.
- There is no salt-and-pepper noise since the pixels with similar spectral properties are segmented into objects.

Disadvantages

- It is computationally expensive and memory-inefficient to work with large areas and high-resolution satellite imagery.
- OBIA is sensitive to segmentation parameters, and it is challenging to determine optimal parameters for the segmentation.

PBIA is a traditional RS image classification commonly used in supervised and unsupervised techniques**.** PBIA classifies individual pixels based on their spectral properties without considering the adjacent pixels. Minimum Distance, Maximum Likelihood, and Spectral Angle Mapping are a few of the common algorithms available in many GIS software for PBIA approaches.

Advantages

- PBIA is simple, straightforward, and demands less computation.
- It captures fine-scale spectral variations.
- It is an established image analysis with mature algorithms and techniques.

Disadvantages

- PBIA is sensitive to noise, such as atmospheric and environmental conditions.
- In contrast to OBIA, PBIA lacks spatial context and makes it ineffective in heterogeneous landscapes.
- It is also challenging for PBIA to classify mixed pixels accurately without considering the spatial patterns.

2.5.Conclusion

Integration of ML and RS data/techniques has been proven to be more efficient and achieved higher accuracy in land cover classification [29, 30, 56] compared to conventional methods [31], and more robust than parametric methods in dealing with complex feature spaces [32]. The selection of an ML algorithm incorporating RS techniques to enhance the land cover classification is crucial. In addition, classifying the land cover with a sole ML algorithm without comparing the result with other ML algorithms is not recommended [57].

In this research, a comparative analysis of ML algorithms for land cover classification was conducted with RF and SVM classifiers using GEE, to identify the most appropriate LULC approach and classifier for land cover classification in the study area and forest regions with similar characteristics. RF and SVM algorithms are commonly used for land cover classification and produce highly accurate compatible results. Considering the time constraints of this research, XGBoost and Deeplabv3+, which require processing outside of GEE were not included in this research.

3. Implementation

3.1. Google Earth Engine (GEE)

Google Earth Engine (GEE)[2] is a cloud-based geospatial analysis platform developed by Google. It enables users to visualize and analyze satellite imagery from several sources, including historical Earth images from forty years ago. The advantages of retrieving and processing satellite imagery on GEE streamline the process, as downloading and storing the raw data locally is no longer necessary, which further enhances the processing time.

In this research, GEE was used as the core platform for data collection, pre-processing, and processing for the entire analysis to achieve the research objectives. A Google Cloud project was created on Earth Engine Code Editor[3] via the web-based Integrated Development Environment (IDE). Google offers academic users and researchers access to this IDE for free. The scripts developed in this research were adapted from GEE Guide[4] to achieve the objectives. Performing various functions in the IDE by scripting eased the experiments in this research, unlike running various tools in GIS environments.

3.2. QGIS software

QGIS[5] is a free open-source professional GIS software that supports Windows, macOS, and Linux. It allows users to manipulate, visualize, and publish geospatial information. Additionally, QGIS allows users to install different plug-in extensions, scripts, and tools from multiple sources that gain the user's access to more functionality. QGIS 3.28 was used in this research to conduct spatial analysis, compute the post-wildfire land cover change, and present map visualization based on the outputs generated by the proposed approach using GEE.

[2] https://earthengine.google.com/faq/
[3] https://code.earthengine.google.com/
[4] https://developers.google.com/earth-engine/guides/
[5] https://www.qgis.org/en/site/

4. Study area

The Serra da Estrela Natural Park (PNSE), shown in Fig. 3, is a natural park with the highest mountain range in the central east of Continental Portugal and is also the largest protected area in the nation. The PNSE spans 89,132.21 hectares across nine municipalities of Belmonte, Celorico da Beira, Covilhã, Fornos de Algodres, Gouveia, Guarda, Manteigas, Oliveira do Hospital and Seia [62]. The largest element of the Central Cordillera is the Tower, with the highest point at 1,991 meters altitude [28], where over half of the natural park area is above 700 meters altitude (Fig. 3).

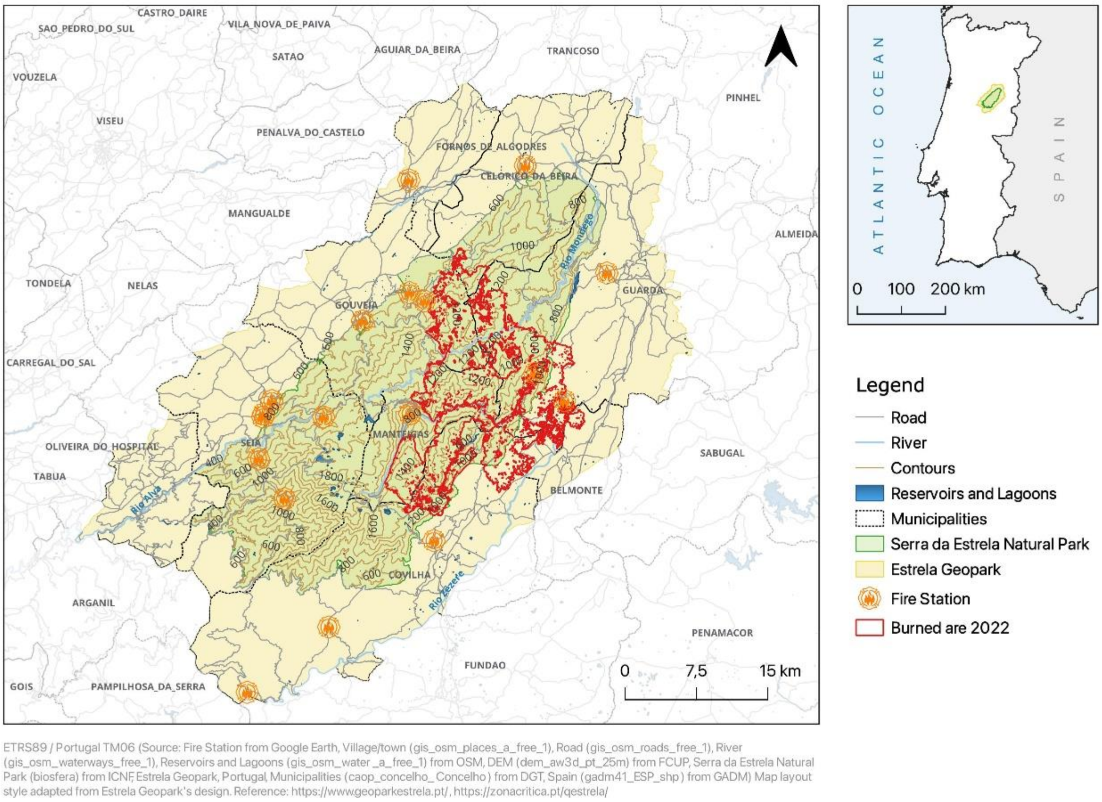

Figure 3. Serra da Estrela Natural Park. (Source: Fire Station from Google Earth, Road/River/Reservoirs and Lagoons from OSM, DEM from FCUP, PNSE boundaries from ICNF, Estrela Geopark/Municipalities from DGT, Spain from GADM)

The PNSE's biodiversity thrives across three climate types – Mediterranean, Atlantic, and Continental, distributed over three altitudinal floors: basal, intermediate, and higher [28]. Its unique topography and climate foster exclusive species, subspecies, and varieties of flora and fauna. The mountain areas in the PNSE shelter endemic species of flora and fauna, some of which only exist in this territory but nowhere else in the world, owing to its altitude and geographic isolation.

The importance of the PNSE was officially recognized as a Natural Park in July 1976; the Natura 2000 Network, with the creation of the Site of Community Interest (SCI) of Serra da Estrela; and 10,610 hectares of the Upper Plateau and the Zêzere Glacier Valley was designated by the Council of Europe as a Biogenetic Reserve in 1993 [63].

In addition, UNESCO recognizes the PNSE as a geopark, Estrela Geopark, for its remnants of the last glaciation, which occurred 30 thousand years ago, and rocks aged up to 600 million years, which present high geodiversity [28]. Estrela Geopark, which occupied an area of 2216 km^2 surrounding the PNSE (Fig. 3), boasts a diverse landscape that is a testament to multiple geological transformations, climatic contrasts, and ancient human settlement, with the first records dating back to the beginning of the fourth millennium B.C. This made Estrela a territory of strong contrasts, where its landscape, both tangible and intangible, reflects a prolonged process of adaptation and successive transformations. The rugged terrain makes it inhospitable for human occupation, which shapes the natural park biodiversity and is safe for the diversity of species of flora and fauna [64]. Overall, the PNSE plays an important role in biodiversity and nature conservation on an international scale.

In this research, the land cover changes of the major burned area affected by the 2022 wildfire in the PNSE were analyzed. The 2022 wildfire started on 6 August 2022 and ended on 2 September 2022 [27]. Sentinel 2A imagery was used to measure the Difference Normalized Burn Ratio (dNBR) to identify the major burned area in the PNSE post-wildfire 2022 for further analysis. The study area covers the burned area beyond the PNSE to the Estrela Geopark (highlighted in red, in Fig. 3), which occupied 24,238.62 hectares.

5. Methodology

This chapter outlines the step-by-step approach (Fig. 4) applied to compare RF and SVM algorithms, with the processing primarily conducted on the GEE platform, for land cover classification and burned area recovery detection in the study area. The approach begins with data acquisition and pre-processing, followed by feature extraction using Red Green Blue (RGB) composition and NDVI results. The feature collections were then processed with PBIA and OBIA for land cover classification. Subsequently, the samples were further split to train/test set to train the classifiers for land cover classification in the region of interest (ROI). The accuracy of the final land cover classification was assessed with evaluation metrics and validation techniques. The land cover maps with the highest accuracy were exported to QGIS for further spatial analysis, burned area recovery detection, and map visualization.

5.1. Data Acquisition and Pre-Processing: Sentinel-2A Imagery

Sentinel-2A imagery was acquired from 'COPERNICUS/S2_SR_HARMONIZED'[6] Image Collection using *ee.ImageCollection* function on GEE. Level-2A imageries are orthorectified atmospherically corrected surface reflectance where the effects of the atmosphere on the light being reflected from the surface of the Earth and reaching the sensor are excluded [65]. Three imageries were selected by filtering the ROI, relevant date range, and cloud coverage below 10% using *ee.ImageCollection.filterBounds()*, *ee.ImageCollection.filterDate()*, and *ee.Filter.metadata()* on GEE, respectively. A buffer area around the major burned area (Fig. 3) was drawn as the ROI to include the neighboring spatial features, enhancing accuracy for the OBIA approach. Images before and after the 2022 wildfire and an image in the summer of 2023 were acquired for comparison consistency to observe the vegetation recovery in the same season. All 12-unit bands in Sentinel-2A imagery were selected, while B1 and B9 were excluded as they are relevant for atmospheric study instead of land surface study, and there is no B10 in

[6] https://developers.google.com/earth-engine/datasets/catalog/COPERNICUS_S2_SR_HARMONIZED

Level-2A imagery. Table 1 shows the usage of the downloaded Sentinel-2A imageries, while Table 2 shows the Sentinel-2 bands with their respective central wavelengths.

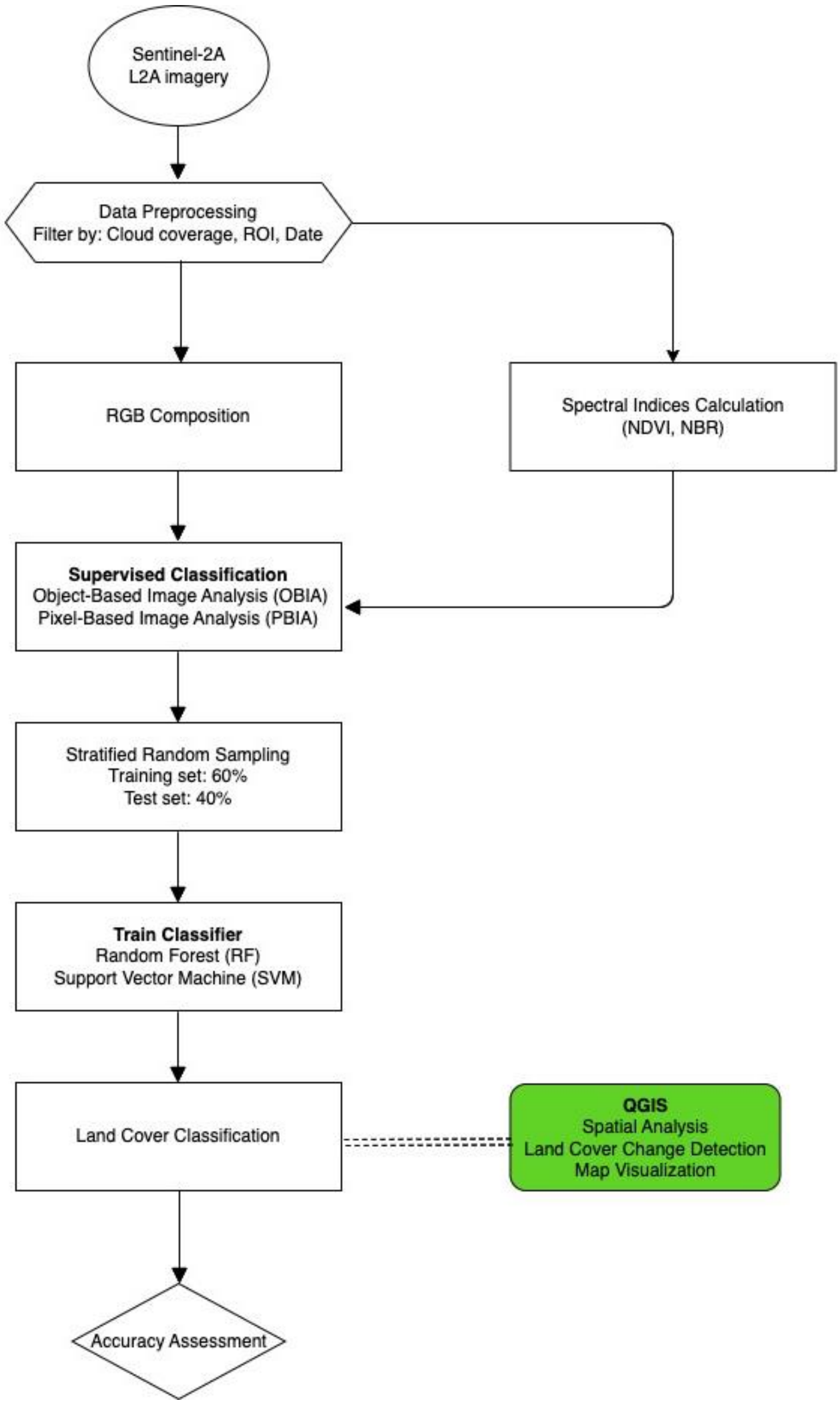

Figure 4. Methodology diagram.

Table 1. Sentinel-2A imagery applied in this research.

Acquisition Date	Event	Image ID
2 August 2022	Pre-wildfire 2022	COPERNICUS/S2_SR_HARMONIZED/20220802 T112119 20220802T112118 T29TPE
26 September 2022	Post-wildfire 2022	COPERNICUS/S2_SR_HARMONIZED/20220926 T112121_20220926T112411_T29TPE
28 July 2023	Summer 2023	COPERNICUS/S2_SR_HARMONIZED/20230728 T112119 20230728T112118 T29TPE

5.2.Spectral Indices

Spectral indices were performed with *ee.Image.normalizedDifference()* on GEE for both Normalized Burn Ratio (NBR) and Normalized Difference Vegetation Index (NDVI).

5.2.1.Normalized Burn Ratio (NBR)

Normalized Burn Ratio (NBR) was computed to detect the burned area before and after the 2022 wildfire in the ROI. The difference between both NBRs was measured to observe the fire severity of the 2022 wildfire. The polygon of the major burned area derived from dNBR before and after the 2022 wildfire was exported to be used as the scope of the study area for further analysis in this research. The fire severity of the major burned area in the ROI was classified according to the dNBR values range proposed by Mediterranean local conditions (MLC) [66], and United States Geological Survey (USGS)[7].

$$\mathbf{NBR = (NIR - SWIR) / (NIR + SWIR)} \quad (1)$$

$$\mathbf{dNBR = NBRprefire - NBRpostfire} \quad (2)$$

Source: Sentinelhub[8]

[7] https://www.un-spider.org/advisory-support/recommended-practices/recommended-practice-burn-severity/in-detail/normalized-burn-ratio
[8] https://custom-scripts.sentinel-hub.com/custom-scripts/sentinel-2/nbr/

Table 2. Spectral bands for Sentinel-2A.

Band	Band Name	Wavelength (nm)	Spatial Resolution (m)
B2	Blue	496.6	10
B3	Green	560	10
B4	Red	664.5	10
B5	Red Edge 1	703.9	20
B6	Red Edge 2	740.2	20
B7	Red Edge 3	782.5	20
B8	NIR	835.1	10
B8A	Narrow NIR	864.8	20
B11	SWIR 1	1613.7	20
B12	SWIR 2	2202.4	20

5.2.2.Normalized Difference Vegetation Index (NDVI)

Normalized Difference Vegetation Index (NDVI) is one of the most used vegetation indices to quantify green vegetation and monitor vegetation health in agriculture, forestry, and ecology. In this research, NDVI was measured to observe the vegetation dynamics between pre-wildfire 2022, post-wildfire 2022, and summer 2023. The results provide valuable information for vegetation loss after the 2022 wildfire and vegetation recovery in summer 2023. Healthy vegetation has more chlorophyll and reflects more NIR, while unhealthy plants reflect more red light. Hence, the formula for NDVI calculation is as below. Subsequently, the NDVI was classified according to the NDVI values range proposed by USGS[9].

[9] NDVI values range (https://www.usgs.gov/special-topics/remote-sensing-phenology/science/ndvi-foundation-remote-sensing-phenology)

$$\mathbf{NDVI = (NIR - Red) / (NIR + Red)} \quad (3)$$

Source: Sentinelhub[10]

5.3.Spectral Analysis and Land Cover Classes

The study area covers land cover of 15 classes at level 3 and 6 classes at level 1, referring to COSc[11]. Referring to COSc 2021 and 2022, shrub and spontaneous herbaceous vegetation were prominent land covers in the study area. It was relatively difficult to distinguish them at level 3 due to their remarkably similar spectral reflectance (Fig. 5). Furthermore, it is challenging to classify the land cover classes as detailed as at level 3 solely based on RGB composition and NDVI results. In addition, Ma et al. studied that large size of classes will reduce the classification's accuracy [67]. Hence, features with high correlation were merged based on their COSc classes at level 1 for further analysis in this research.

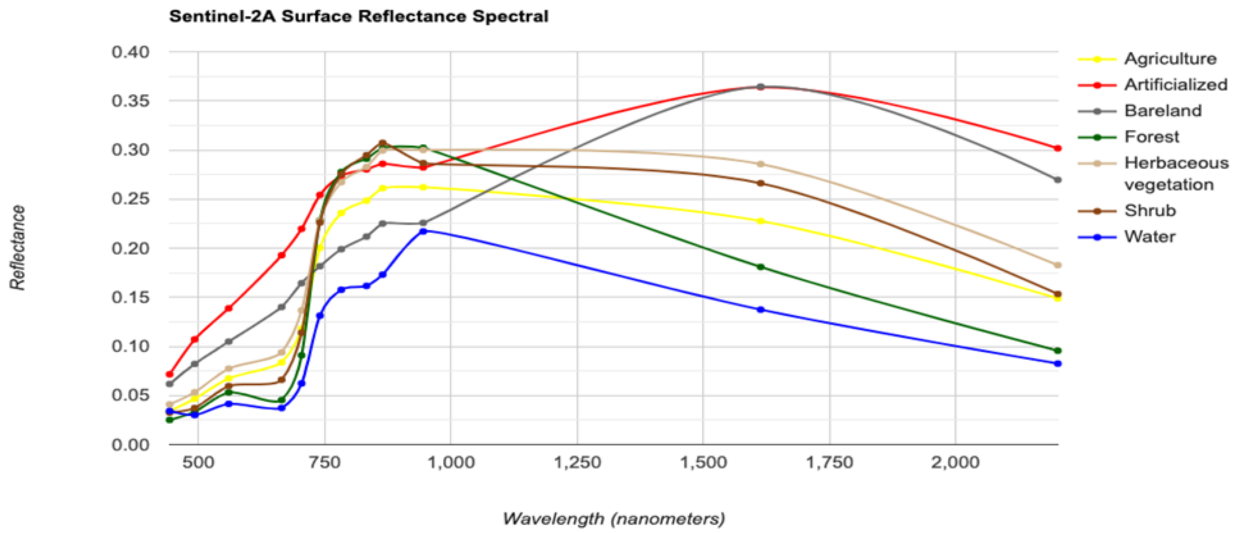

Figure 5. Spectral reflectance of different land cover classes in the burnt area pre-wildfire 2022.

[10] https://custom-scripts.sentinel-hub.com/custom-scripts/hls/ndvi/
[11] COSc: https://www.dgterritorio.gov.pt/sites/default/files/documentos-publicos/Nomenclatura_COSc.pdf

Table 3. Description of the 6 land cover classes used in this research.

ID	Class/Level 1	Level 3	Satellite image
0	2 - Agriculture	211- Autumn/winter annual crops 212 - Spring/summer annual crops 213 - Other agricultural areas	
1	1 - Artificial	100 - Artificial areas	
2	5 - Bareland	500 - Surface without vegetation	
3	3 - Forest	311 - Cork oak and holm oak 312 - Eucalyptus 313 - Other hardwoods 321 - Maritime pine 323 - Other resinous plants	
4	4 - Shrub	410 - Shrub 420 - Spontaneous herbaceous vegetation	
5	6 - Water	620 - Water	

5.4. Dataset Creation

PBIA and OBIA are widely used for land cover classification in RS applications. In this research, RGB composition and NDVI results were referred interactively to collect the features manually. The features were drawn in polygon because point-based samples tend to be more unstable [67]. Subsequently, the features were grouped into six (6) feature collections as categorized in chapter 5.3. As sample size does not guarantee dataset accuracy [67], 100 features were collected for all land cover classes, except for class **5. Water**, which occupied an insignificant area within the ROI. The six (6) feature collections were combined into a single feature collection using *ee.FeatureCollection()* function to unify all samples of all the land cover classes for data training and validation purposes. Images were sampled at 20 m resolution for both PBIA and OBIA approaches using *ee.Image.sampleRegions()*. The scale parameter was set at 20 m resolution after some experiments. A lower scale was computationally expensive and tended to be overfitting the samples.

5.4.1. Pixel-Based Image Analysis (PBIA)

PBIA classification was performed with different classifiers on GEE for land cover classification in urban [68] and forest areas [69]. These models produced land cover classification with satisfactory accuracy, which justified the inclusion of the PBIA approach in this study in developing the best model to classify the land cover in the study area.

5.4.2. Object-Based Image Analysis (OBIA)

Simple Non-Iterative Clustering (SNIC) algorithm on GEE was used for OBIA segmentation in this research (Appendix A). SNIC is a bottom-up, seed-based segmentation algorithm that groups neighbouring pixels based on spatial data and proximity similarity into clusters. The seeds are the initial points where the clusters grow and spaced evenly across the image based on the parameter set. As there were large homogeneous areas, such as forest and bare land, and fine details, such as artificial areas, shrublands, and water, a balance between the grid spacing is vital. After some experiments, the parameter of 20 pixels was set for the spacing between seeds to be able to capture the feature details while not over-segmenting the image. The grid's shape was set to hexagonal, to minimize the distances and increase the uniform distribution between neighboring seeds. The compactness was set to 0 to enable accurate segmentation based on the intrinsic characteristics (spectral and textural features) instead of the spatial proximity due to the diversified classes and irregular shape of land cover in the study area [70].

5.5.Classification

The samples generated with PBIA and OBIA approaches were split into training and test datasets in a 60:40 ratio using *ee.ImageCollection.randomColumn().* This provided datasets to train RF and SVM algorithms for land cover classification through stratified random sampling. After testing datasets with different tree sizes, the parameter was set to 30 for the RF classifier to optimize the land cover classification using *ee.Classifier.smileRandomForest()*. For the SVM classifier, the default setting of *ee.Classifier.libsvm()* on GEE was employed. The default Radial Basis Function (RBF) kernel was effective for a wide range of classification tasks, including land cover classification [72-74], while Yousefi et al. studied that variation of the gamma values did not affect the accuracy of the land cover classification [71]. Subsequently, the trained classifiers were applied to classify the land cover of the three imageries. Hence, four (4) models were applied to each imagery which produced twelve (12) land cover maps in total: (a) RF x OBIA, (b) RF x PBIA, (c) SVM x OBIA, and (d) SVM x PBIA. All the land cover maps were *reprojected* to EPSG:3763.

5.6.Accuracy Assessment

The land cover maps produced by different models, integration of LULC classifications (PBIA or OBIA), and classifiers (RF or SVM) were assessed and compared to identify the best model for land cover classification in the study area. Evaluation metrics include (a) confusion matrix, (b) F1 score, (c) OA, and (d) kappa coefficient, which were conveniently performed using *ee.ConfusionMatrix* functions. Due to a lack of ground truth data that is comparable to the outputs of this research, land cover maps were compared with NDVI maps for the pre-wildfire 2022 results, burned area 2022 from ICNF and dNBR maps for the post-wildfire 2022 results, and COSc 2023 from SNIG for summer 2023 results.

5.6.1.Confusion Matrix

Confusion matrix was performed using *ee.ConfusionMatrix()* function. True positive (TP) is the assignment where the model correctly predicts the land cover classes while true negative (TN) is the assignment where the model is indeed assigned the land cover classes wrongly. On the other hand, commission error (false positive/FP) is a sample wrongly assigned to other land cover classes that it does not belong to, while omission error (false negative/FN) is a sample left out in the land cover class that it is supposed to be assigned. The values generated in confusion matrix were further evaluated for precision and recall values which were performed with *consumersAccuracy()* and *producersAccuracy()* on GEE, respectively.

$$\textbf{Precision = TP / (TP + FP)} \tag{4}$$

$$\textbf{Recall = TP / (TP + FN)} \tag{5}$$

5.6.2.F1 Score

While precision and recall values of different land cover classes might be inconsistent in accuracy ranking, the F1 score was measured to obtain an insight into the accuracy of each model in classifying the land cover classes. F1 score balances precision and recall by minimizing FP and FN. F1 score has a value from 0 to 1, where 1 indicates perfect precision and recall while 0 means otherwise. The measurement was conducted using *ee.ConfusionMatrix.fscore()* on GEE.

F1 score = 2 * [(precision * recall) / (precision + recall)] (6)

5.6.3. Overall Accuracy

Overall accuracy (OA) provides an overview of the overall accuracy of TP and TN to the total assignments. OA has a value range between 0 and 1, where 1 represents the highest accuracy while 0 shows no accuracy. The measurement was conducted using *ee.ConfusionMatrix.accuracy()* on GEE.

Overall accuracy (OA) = (TP + TN) / (TP + TN + FP + FN) (7)

5.6.4. Kappa Coefficient

Kappa coefficient indicates the inter-rater reliability between the land cover classification. The degree of agreement ranges between –1 to 1, where 1 represents perfect agreement, 0 represents no agreement, and –1 represents an agreement that is worse than random. The Kappa coefficient was measured using *ee.ConfusionMatrix.kappa().*

$$\text{Kappa Coefficient (T)} = \frac{(TS * TCS) - \sum(Column\ Total \times Row\ Total)}{TS^2 - \sum(Column\ Total \times Row\ Total)} \times 100 \qquad (8)$$

where TS = total number of samples, TCS = total number of correctly assigned samples

Source: Carleton University[12]

[12]https://dges.carleton.ca/CUOSGwiki/index.php/Random_Forest_Supervised_Classification_Using_Sentinel-2_Data#Contingency_Table_and_Kappa_Coefficient_Analysis

5.6.5. Burned Territories - Burned Area 2022 and dNBR

The burned territories - burned area 2022[13] (BA 2022), prepared by the Institute for Nature Conservation and Forests (ICNF), was retrieved for land cover classification validation purposes. The extent of the major burned area, derived from the difference in NBR before and after the 2022 wildfire, was compared with BA 2022 to validate the burned area extent after the wildfire event. As BA22 lacks robustness to assess the land cover maps, the dNBR map was referred to analyze the rationality of post-wildfire land cover change relative to fire severity.

5.6.6. NDVI Map

NDVI map generated for the pre-wildfire event was compared with the land cover maps classified by different models for the same event. This was to assess if the land size of the land cover reflected the vegetation conditions of the study area and examine the spatial data's consistency.

5.6.7. COSc

COSc 2023[14] were obtained from SNIG to compare with land cover maps of summer 2023. COSc 2023 was classified based on a spectral database of monthly mean in addition to spectral indices and intra-annual metrics from October 2022 to September 2023. The training database is processed with auxiliary information and photointerpretation and further classified with space technologies and artificial intelligence. The land cover classes in COSc 2023 were visualized at COSc level 1, as illustrated in chapter 5.3, to make the maps comparable.

[13] https://sig.icnf.pt/portal/home/item.html?id=983c4e6c4d5b4666b258a3ad5f3ea5af
[14] https://snig.dgterritorio.gov.pt/rndg/srv/eng/catalog.search#/metadata/e9d25fc4-5a25-4c5e-9bce-d470f745d89e?tab=metainfo

5.7.Land Cover Change Detection

The land cover maps generated by the models were exported to QGIS for further analysis. The land cover maps were first *clipped* with the major burned area extent. Descriptive statistics of NDVI and NBR, land area size according to spectral indices and land cover classes of the study area were computed. Land cover maps of the study area's pre-wildfire 2022, post-wildfire 2022, and summer 2023 were *intersected* to detect the land cover change. The results were visualized in maps while the area size of major land cover change of each class was presented in tables. All the land cover maps are attached in Appendix D and are labelled according to their model and event in the following order: (a) the classifier, (b) the LULC classification approach, and (c) the event, e.g., RF_OBIA_S22. The labels are abbreviated as RF – Random Forest, SVM – Support Vector Machine, PBIA – pixel-based image analysis, OBIA – object-based image analysis, S22 – pre-wildfire 2022, F22 – post-wildfire 2022, and S23 – summer 2023.

6. Results

6.1. Spectral indices

6.1.1. Difference Normalized Burn Ratio (dNBR)

The study area primarily experienced moderate and high degree of fire severity in the 2022 wildfire, according to dNBR classification proposed by both MLC and USGS (Fig. 6). As shown in Table 4, 49.23% and 12.05% of the study area experienced moderate and low degree of fire severity according to USGS's classification while 43.03% and 16.89% of the study area experienced moderate and low degree of fire severity according to MLC's classification. The differences in area size found were due to the significant difference in classification values range proposed by MLC and USGS in low and moderate degrees of fire severity. Unburned areas and areas affected by a high degree of fire severity occupied around 2% and 37%, respectively, in both classifications.

Table 4. Analysis of the land area affected by different fire severities in the study area after the 2022 wildfire, based on the dNBR ranges proposed by MLC and USGS.

Fire Severity	dNBR range (scaled by 10^3)	MLC ($100m^2$)	%	dNBR range (scaled by 10^3)	USGS ($100m^2$)	%
Unburned	<= 100	53291	2.20	<= 100	53291	2.20
Low	100 - 320	409450	16.89	100 - 270	292044	12.05
Moderate	320 - 650	1042929	43.03	270 - 660	1193272	49.23
High	> 650	918192	37.88	> 660	885255	36.52
Total		2423862	100		2423862	100

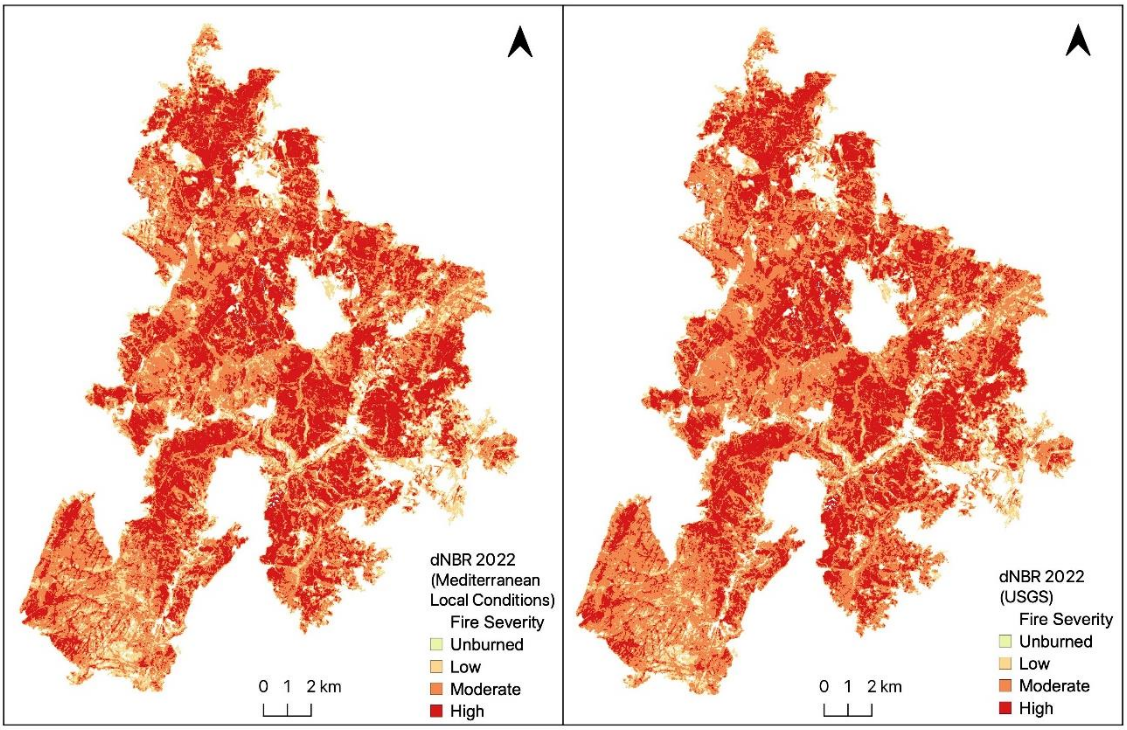

Figure 6. The dNBR maps of the study area for the 2022 wildfire, based on classifications proposed by MLC (left), and UGSG (right).

6.1.2.Normalized Difference Vegetation Index (NDVI)

Fig. 7 reflects the vegetation dynamic of the study area between pre-wildfire 2022, post-wildfire 2022, and summer 2023. It indicates that the study area was predominantly occupied by dense vegetation before the wildfire event. As about 98% of the study area experienced low to high fire severity (Table 4) during the 2022 wildfire, the area was occupied with sparse vegetation and had little dense vegetation after the wildfire. On the NDVI map of summer 2023 (Fig. 7), vegetation recovery was observed, especially in the top north of the study area. As shown in Table 5, the land area size of dense vegetation validated the vegetation dynamic of the study area along the events where dense vegetation occupied 65.12% of the study before the wildfire, reduced to 7.04% after the wildfire, and recovered to 23.84% in summer 2023. Meanwhile, the sparse vegetation increased from 34.85% to 91.98% after the 2022 wildfire and reduced to 75.11% in the summer of 2023. The area with no vegetation within the study area

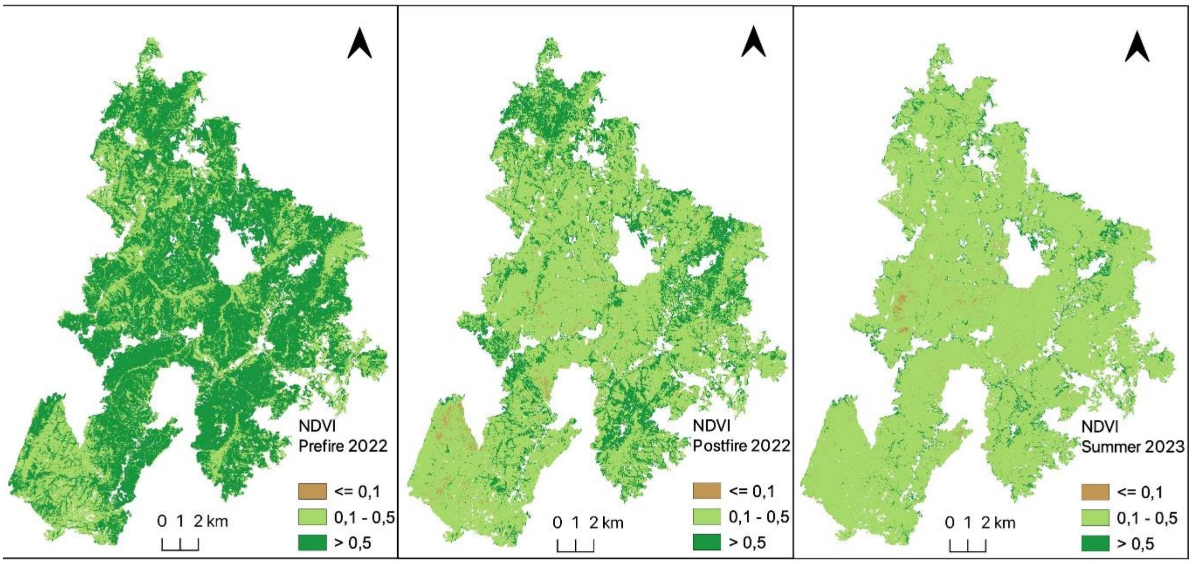

Figure 7. NDVI maps of the study area for: (a) pre-wildfire 2022, (b) post-wildfire 2022, and (c) summer 2023, computation was made from Sentinel-2A data.

Table 5. Analysis of the study area size subject to NDVI values range suggested by USGS.

NDVI	Pre-wildfire 2022 ($100m^2$)	%	Post-wildfire 2022 ($100m^2$)	%	Summer 2023 ($100m^2$)	%
<= 0.1	647	0.03	23563	0.98	25378	1.05
0.1 - 0.5	844708	34.85	2229573	91.98	1820739	75.11
> 0.5	1578507	65.12	170726	7.04	577745	23.84
Total	2423862	100	2423862	100	2423862	100

remained around 1% and less in any events. Further analysis was conducted after the unusually high NDVI value found in the descriptive statistic of post-wildfire events, as shown in Table 6. This can be misleading, as it suggests dense vegetation presence within the burned area following the 2022 wildfire. An analysis with a smaller NDVI values range was conducted to discover the land area size of high NDVI values. The NDVI value higher than 0.9 was found to occupy only an immaterial size of 0.02% of the study area. In addition, these areas were mainly clustered along the perimeter of the burnt area. The map visualization and descriptive statistics table are consultable in Appendix B.

Table 6. Descriptive statistics of NDVI for pre-wildfire 2022, post-wildfire 2022, and summer 2023 in the study area.

NDVI	Pre-wildfire 2022	Post-wildfire 2022	Summer 2023
Minimum	0.0650	-0.4845	-0.0514
Maximum	0.9549	0.9336	0.9316
Mean	**0.5668**	**0.2578**	**0.3676**
Standard dev.	0.1845	0.1347	0.1878

6.1.3.Difference Normalized Difference Vegetation Index (dNDVI)

The difference Normalized Difference Vegetation Index (dNDVI) maps, derived from the difference between NDVI of post-wildfire and pre-wildfire events, and NDVI of summer 2023 and post-wildfire 2022 are consistent with the temporal analysis of the vegetation dynamics across these events as observed in Fig. 7. As shown in Fig. 8, red color indicates vegetation loss after 2022 wildfire on map (a), while green color indicates vegetation regeneration in summer 2023 on map (b).

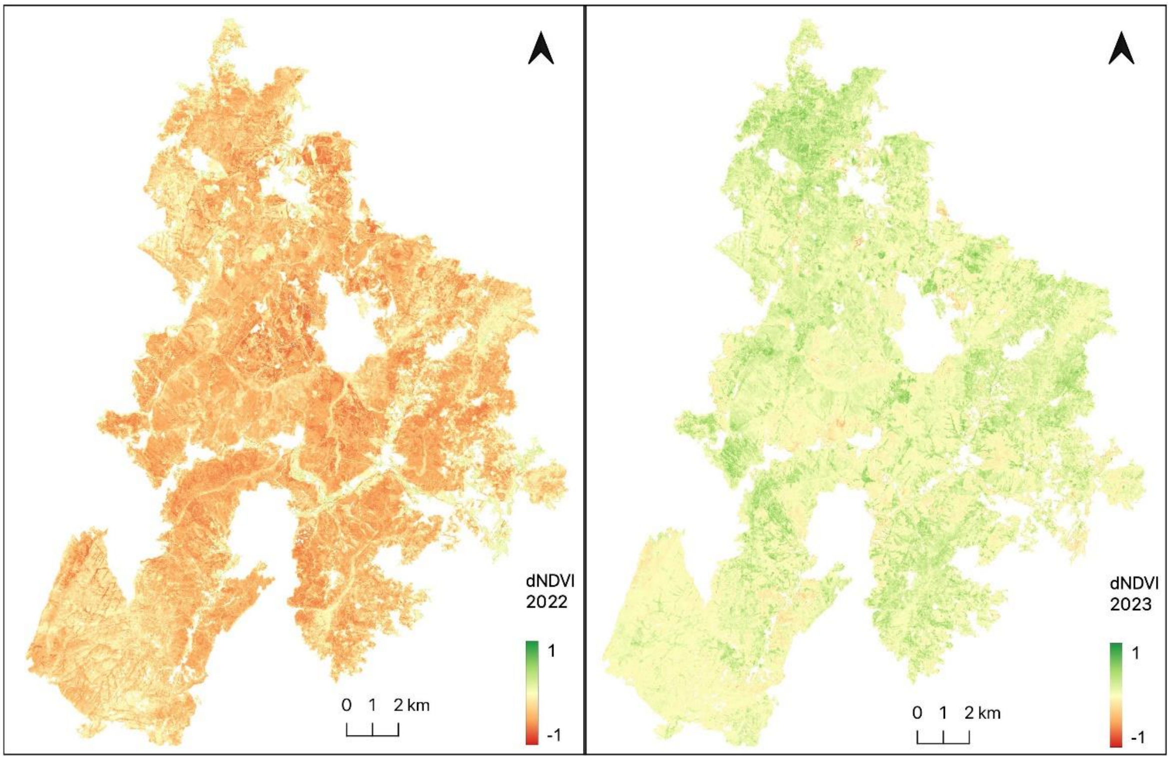

Figure 8. The dNDVI maps of the study area for: (a) dNDVI 2022, and (b) dNDVI 2023.

6.2.Evaluation Metrics for Random Forest and SVM

6.2.1.Confusion Matrix

Table 7 to Table 9 present the confusion matrix table of the model with the highest accuracy for each event, while the matrix tables of other models are available in Appendix C. It shows that the RF x OBIA model achieved the highest accuracy in land cover classification for the study area in all events. As shown in Table 7 to Table 9, this model is capable of distinguishing different land cover classes in all events, except for **4. Shrub**. The confusion matrix tables in Appendix C show that class **4. Shrub** was always misclassified with **0. Agriculture** interchangeably, particularly with models using PBIA approach. The misclassification in the post-wildfire result produced by the SVM x PBIA model was weighty, where 223 samples were misclassified as **0. Agriculture**. This has far exceeded the 83 samples that were classified correctly for **4. Shrub** (Table C6). Consequently, classification of **4. Shrub** and **0. Agriculture** achieved a precision value of 0.2602 and a recall value of 0.6459, respectively, in this event (Table C6). However, the

Table 7. Confusion Matrix of RF x OBIA model [pre-wildfire 2022].

RF x OBIA	0	1	2	3	4	5	**Precision**
0	1109	3	0	0	13	0	0.9858
1	0	338	0	0	4	0	0.9883
2	6	1	1130	0	2	0	0.9921
3	0	0	4	2597	2	0	0.9977
4	18	16	1	13	749	0	0.9398
5	0	0	0	0	0	72	1
Recall	0.9788	0.9441	0.9956	0.995	0.9727	1	

Table 8. Confusion Matrix of RF x OBIA model [post-wildfire 2022].

RF x OBIA	0	1	2	3	4	5	**Precision**
0	1141	0	0	0	11	0	0.9905
1	0	208	0	1	22	0	0.9004
2	0	0	2586	0	0	0	1
3	0	0	5	1014	1	0	0.9941
4	2	11	4	3	284	0	0.9342
5	0	0	0	0	0	49	1
Recall	0.9983	0.9498	0.9965	0.9961	0.8931	1	

Table 9. Confusion Matrix of RF x OBIA model [summer 2023].

RF x OBIA	0	1	2	3	4	5	Precision
0	1225	0	0	0	2	0	0.9984
1	1	185	0	0	20	0	0.8981
2	0	2	2299	0	0	0	0.9991
3	0	0	0	2282	2	0	0.9991
4	6	11	0	2	475	0	0.9615
5	0	0	0	0	0	97	1
Recall	0.9943	0.9343	1	0.9991	0.9519	1	

precision and recall value for **4. Shrub** classified by RF x OBIA model was at a satisfactory level. Furthermore, misclassification between **0. Agriculture,** and **3. Forest** was generally noticeable in the PBIA approach. However, land cover classification of pre-wildfire generated by SVM x OBIA model demonstrated 770 samples misclassified as **3. Forest** instead of **0. Agriculture**, resulting in a low precision value of 0.6266 and recall value of 0.4787 for **3. Forest** and **0. Agriculture**, respectively (Table C2).

6.2.2.F1 Score

Table 10 to Table 15 indicate that **5. Water** achieved an F1 score of 1, indicating perfect precision and recall value in all models. This was expected as the spectral reflectance of **5. Water** is significant to other land covers, as observed in Fig. 5. Regardless of the models, **2. Bareland** and **3. Forest** were classified precisely, especially in the RF x OBIA model, where the F1 score was close to value 1 in all events. Classification of **4. Shrub** achieved the lowest F1 score with SVM x PBIA model in all events. While none of the F1 scores were higher than 0.634 with SVM x PBIA model, the classification for **4. Shrub** after the 2022 wildfire achieved the lowest values of 0.3374, 0.2602, and 0.4798 for F1 score, precision, and recall, respectively (Table 13). Furthermore, **0. Agriculture** obtained the lowest F1 score with the SVM classifier in pre-wildfire events, as low as 0.6015 and 0.6151 for the OBIA and PBIA approaches, respectively (Table 11). As noticed in Fig. 9, it is interesting to note that OBIA and PBIA had consistent performance with both RF and SVM classifiers in F1 score ranking for classification in post-wildfire 2022 and summer 2023. Overall, RF has a relatively stable performance compared to SVM, as the accuracy of land cover classification using SVM fluctuated significantly among different scenarios. This was observed from the samples classified for **1. Artificial,** where high accuracy was achieved in the pre-wildfire event while lower accuracy was attained in other events.

Table 10. RF metric results for OBIA and PBIA approach [pre-wildfire 2022].

Dataset	Class	F1 Score	Precision	Recall
RF x OBIA	0	0.9823	0.9858	0.9788
	1	0.9657	0.9883	0.9441
	2	0.9938	0.9921	0.9956
	3	0.9964	0.9977	0.995
	4	0.956	0.9398	0.9727
	5	1	1	1
RF x PBIA	0	0.8283	0.8045	0.8535
	1	0.8996	0.8929	0.9063
	2	0.9262	0.9599	0.8948
	3	0.9477	0.9788	0.9184
	4	0.7668	0.6871	0.8673
	5	1	1	1

Table 11. SVM metric results for OBIA and PBIA approach [pre-wildfire 2022].

Dataset	Class	F1 Score	Precision	Recall
SVM x OBIA	0	0.6015	0.8089	0.4787
	1	0.8663	0.8713	0.8613
	2	0.8585	0.8973	0.8229
	3	0.7616	0.6266	0.9708
	4	0.6916	0.7089	0.675
	5	1	1	1
SVM x PBIA	0	0.6151	0.6206	0.6097
	1	0.9062	0.9196	0.8931
	2	0.8627	0.903	0.8259
	3	0.9045	0.9258	0.8843
	4	0.6027	0.515	0.7264
	5	1	1	1

Table 12. RF metric results for OBIA and PBIA approach [post-wildfire 2022].

Dataset	Class	F1 Score	Precision	Recall
RF x OBIA	0	0.9943	0.9905	0.9983
	1	0.9244	0.9004	0.9498
	2	0.9983	1	0.9965
	3	0.9951	0.9941	0.9961
	4	0.9132	0.9342	0.8931
	5	1	1	1

RF x PBIA	0	0.8812	0.9064	0.8574
	1	0.9716	0.9823	0.961
	2	0.9975	0.9973	0.9977
	3	0.9332	0.9393	0.9272
	4	0.6375	0.5461	0.7656
	5	1	1	1

Table 13. SVM metric results for OBIA and PBIA approach [post-wildfire 2022].

Dataset	Class	F1 Score	Precision	Recall
SVM x OBIA	0	0.8466	0.8741	0.8207
	1	0.844	0.8312	0.8571
	2	0.9977	1	0.9954
	3	0.8988	0.8755	0.9235
	4	0.5577	0.5329	0.5848
	5	1	1	1
SVM x PBIA	0	0.6706	0.6973	0.6459
	1	0.9241	0.9241	0.9241
	2	0.9897	0.988	0.9915
	3	0.7904	0.8144	0.7679
	4	0.3374	0.2602	0.4798
	5	1	1	1

Table 14. RF metric results for OBIA and PBIA approach [summer 2023].

Dataset	Class	F1 Score	Precision	Recall
RF x OBIA	0	0.9963	0.9984	0.9943
	1	0.9158	0.8981	0.9343
	2	0.9996	0.9991	1
	3	0.9991	0.9991	0.9991
	4	0.9567	0.9615	0.9519
	5	1	1	1
RF x PBIA	0	0.8621	0.8835	0.8418
	1	0.7949	0.6889	0.9394
	2	0.9828	0.993	0.9728
	3	0.9758	0.9846	0.9672
	4	0.7393	0.672	0.8215
	5	1	1	1

Table 15. SVM metric results for OBIA and PBIA approach [summer 2023].

Dataset	Class	F1 Score	Precision	Recall
SVM x OBIA	0	0.9555	0.9527	0.9582
	1	0.8565	0.8981	0.8186
	2	0.9993	0.9987	1
	3	0.9825	0.9733	0.992
	4	0.8854	0.915	0.8577
	5	1	1	1

SVM x PBIA	0	0.7452	0.7763	0.7165
	1	0.7793	0.7378	0.8259
	2	0.9706	0.9811	0.9603
	3	0.9253	0.9029	0.9488
	4	0.634	0.622	0.6466
	5	1	1	1

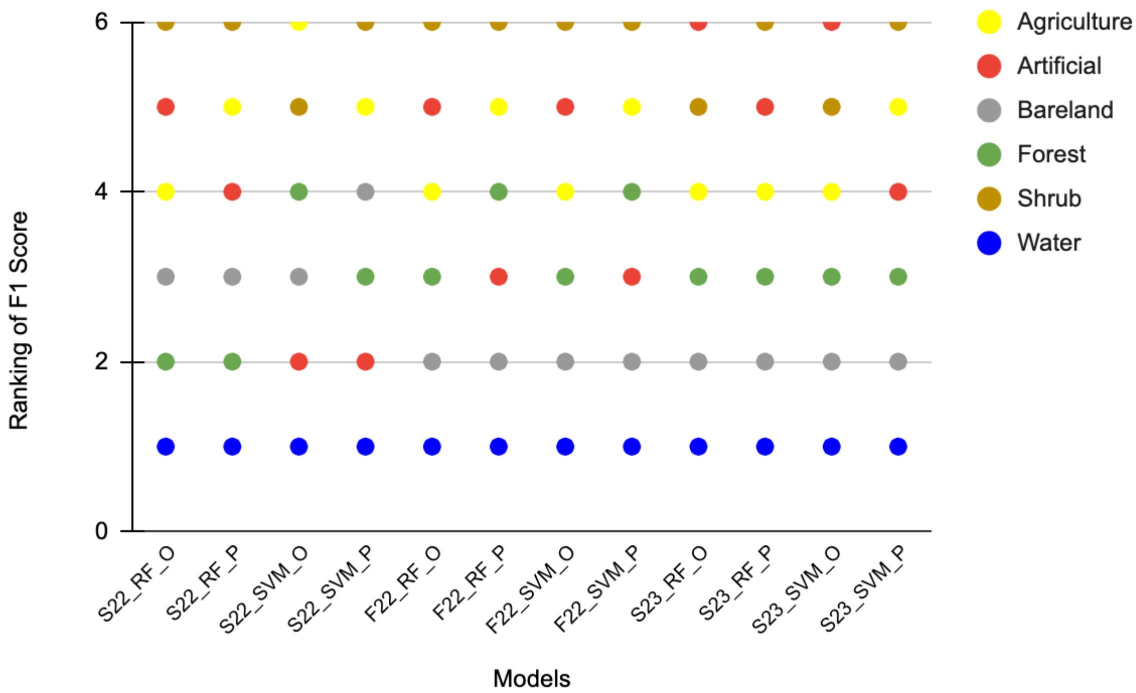

Figure 9. F1 score ranking for different land cover classes across various models.

Notes: 1 (Highest F1 score) to 6 (Lowest F1 score)

6.2.3.Overall Accuracy and Kappa Coefficient

Overall accuracy and kappa coefficient values indicated in Table 16 aligned with the results found in sub-chapter 6.2.2.. RF x OBIA model achieves the highest accuracy where the OA value was 0.99 and the kappa coefficient value was higher than 0.98 in all events. Regardless of the LULC classification approach, the RF classifier achieved higher

OA and kappa coefficient values compared to the SVM classifier in most events, except for summer 2023. SVM x OBIA model attained exceptional accuracy with an OA of 0,97 and a kappa coefficient of 0.96 for land cover classification of summer 2023, outperforming RF x PBIA model. Table 16 shows that the performance of the SVM classifier with both LULC approaches was not stable; one was better than the others in different events.

Table 16. Overall accuracy and kappa coefficient of each model.

	RF x OBIA		RF x PBIA		SVM x OBIA		SVM x PBIA	
	OA	κ	OA	κ	OA	κ	OA	κ
Pre-fire	0.99	0.98	0.90	0.86	0.74	0.66	0.81	0.73
Post-fire	0.99	0.98	0.94	0.91	0.84	0.76	0.85	0.77
Summer	0.99	0.99	0.94	0.91	0.97	0.96	0.88	0.83

6.3.Comparison of Land Cover Classification Accuracy

6.3.1.Comparison with Burned Territories - Burned Area 2022

Land cover maps of post-wildfire 2022, classified by different models, are presented in Fig. 10. The burned territories - burned area 2022 (BA22) shapefile retrieved from ICNF was highlighted in red border (Fig. 10). BA22 and fire severity analysis in Fig. 6 were taken into consideration to assess the accuracy of the land cover maps. The land cover map classified by the RF x OBIA model (top left) reflected the fire severity (Fig. 6) better. Furthermore, Table 17 detailed that 20,512.27 hectares of **2. Bareland** classified by RF x OBIA model is closest to the total area that experienced moderate and high degrees of fire severity, 19,611.21 hectares (MLC) and 20,785.27 hectares (USGS), as presented in Table 4.

Table 17. Analysis of the land cover size after wildfire 2022 for each model.

F22	RF x OBIA		RF x PBIA		SVM x OBIA		SVM x PBIA	
Class	**Area (ha)**	**%**	**Area (ha)**	**%**	**Area (ha)**	**%**	**Area (ha)**	**%**
0	1,655.68	6.83	2,989.13	12.33	3,684.57	15.20	5,172.30	21.34
1	191.49	0.79	373.98	1.54	639.68	2.64	593.50	2.45
2	20,512.27	84.63	18,566.33	76.60	18,710.02	77.19	17,346.21	71.56
3	1,152.91	4.76	1,527.02	6.30	754.61	3.11	391,02	1.61
4	724.23	2.99	779.75	3.22	447.71	1.85	733.09	3.02

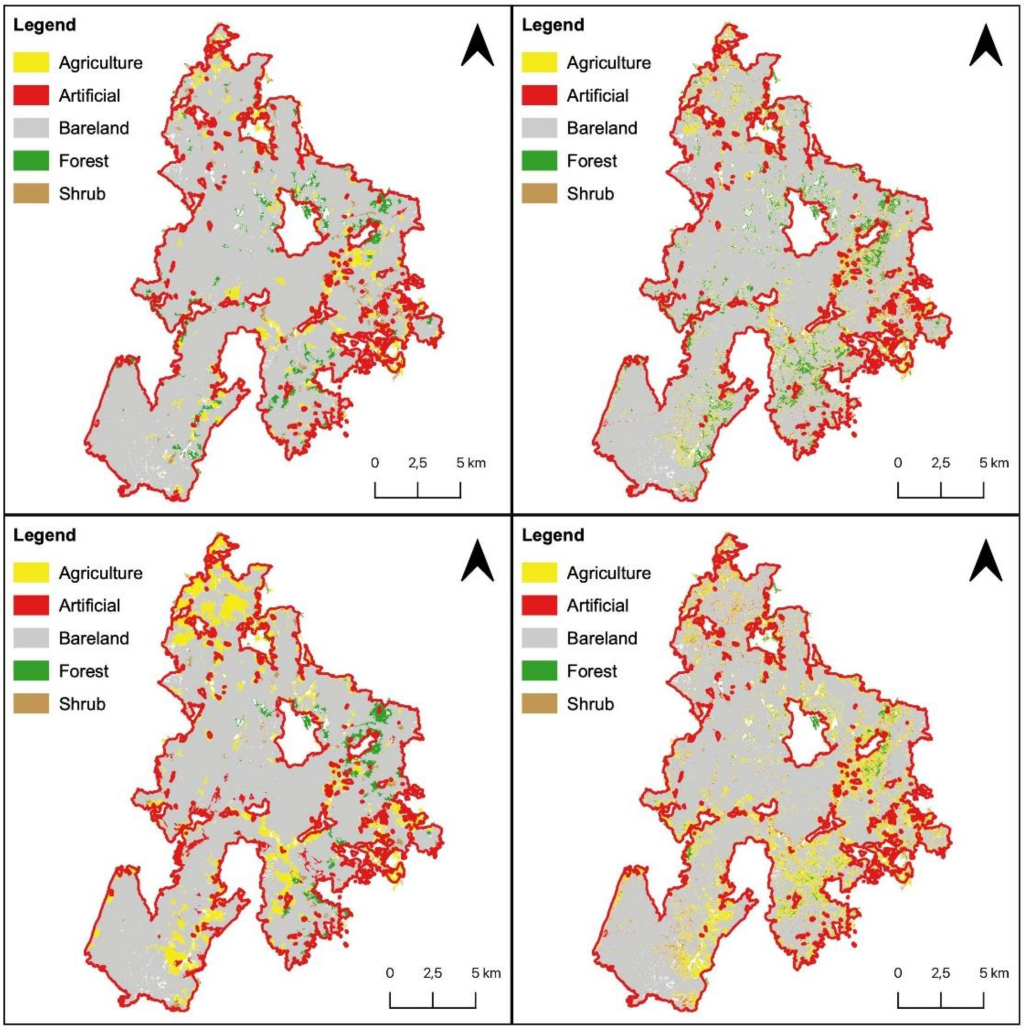

Figure 10. Comparison of the burned area retrieved from ICNF (red border) and the post-wildfire land cover maps classified by different models (top left: RF x OBIA, top right: RF x PBIA, bottom left: SVM x OBIA, top left: SVM x PBIA).

6.3.2.Comparison with NDVI

Fig. 11 presents the land cover maps of pre-wildfire 2022 that were classified by different models. They were compared with the NDVI map of pre-wildfire 2022 (Fig. 7). Land cover maps classified by RF x OBIA (top left) and SVM x PBIA (bottom right) were observed to be more consistent with the NDVI map. Table 5 details the vegetation of the study area before the 2022 wildfire: no vegetation (0.03%), sparse vegetation (34.85%), and dense vegetation (65.12%). In comparison, the PBIA approach was found to have a smaller area of **0. Agriculture, 1. Artificial,** and **2. Bareland**, and larger area for **3. Forest**, and **4. Shrub** compared to the OBIA approach, as shown in Table 18. The land cover map classified by the RF x OBIA model indicates unusual **2. Bareland** area compared to the NDVI map (Fig. 7). In view of the comparison with the NDVI map and analysis of the land cover size, the land cover map classified by SVM x PBIA model reflected the pre-wildfire land cover more precisely.

Table 18. Analysis of the land cover size before wildfire 2022 for each model.

S22	RF x OBIA		RF x PBIA		SVM x OBIA		SVM x PBIA	
Class	Area (ha)	%	Area (ha)	%	Area (ha)	%	Area (ha)	%
0	2,452.94	10.12	1,681.94	6.94	29,298	29.3	5292.29	21.83
1	173.57	0.72	72.32	0.3	236.05	0.97	63.35	0.26
2	2,256.58	9.31	1,055.52	4.36	5,463.7	22.54	984.99	4.06
3	17,846.,91	73.63	18,083.46	74.61	9,405.24	38.8	14884.9	61.41
4	1,506.59	6.22	3,342.97	13.79	2,030.13	8.38	3010.71	12.42

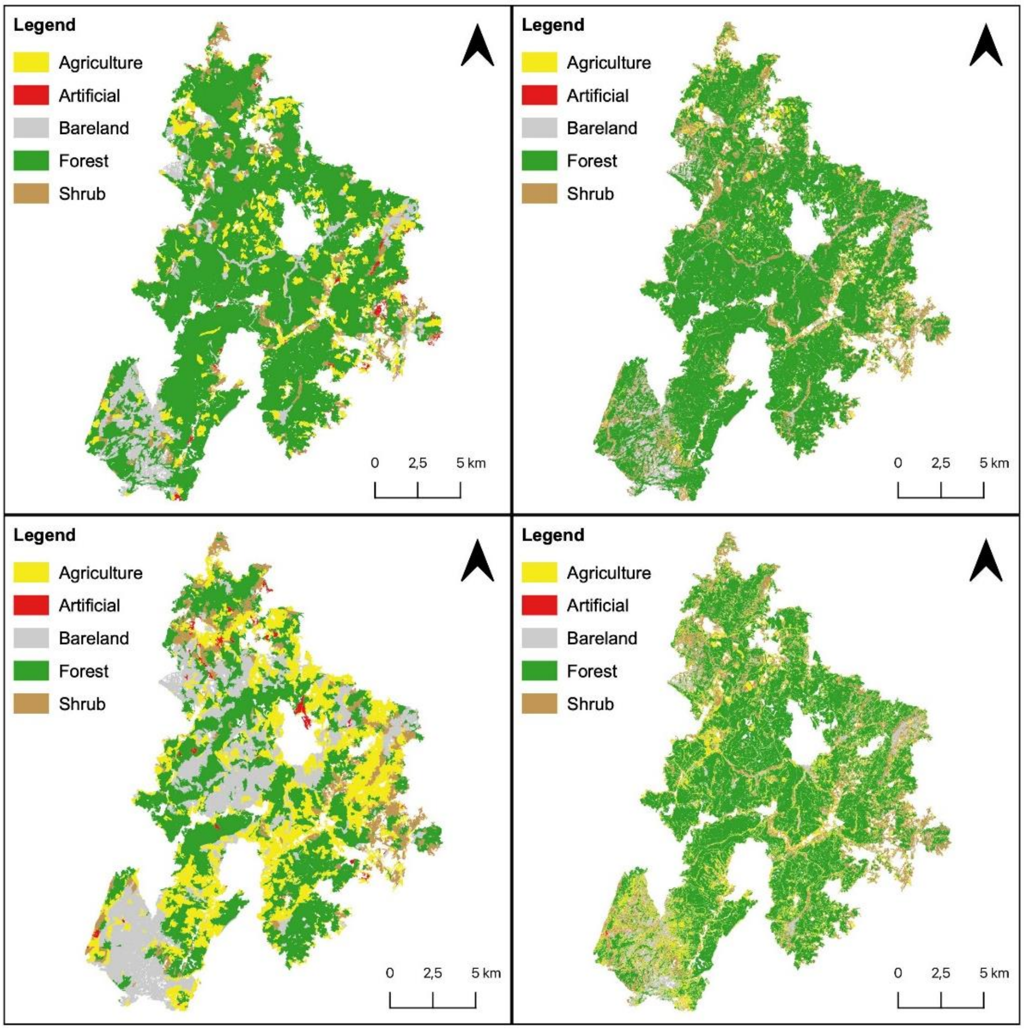

Figure 11. Comparison of land cover maps classified by different models (top left: RF x OBIA, top right: RF x PBIA, bottom left: SVM x OBIA, top left: SVM x PBIA) for pre-wildfire 2022.

6.3.3.Comparison with COSc

According to COSc 2023, the study area was majorly recovered to shrubland with minor agricultural land and forest regeneration while a smaller area of bare land remained (Fig. 12). As compared to Fig. 12, Fig. 13 indicated that land cover maps classified by PBIA approach reflect the burned area recovery and regeneration of forest more precisely. This was further confirmed by the land cover analysis presented in Table 19, in which the land size of bare land and forest classified by the PBIA approach was closer to the COSc 2023 classification, as compared to the land cover maps classified by the OBIA approach. Table 19 details that all models classified a much larger area of agricultural land and artificial land and a much smaller shrubland compared to COSc 2023.

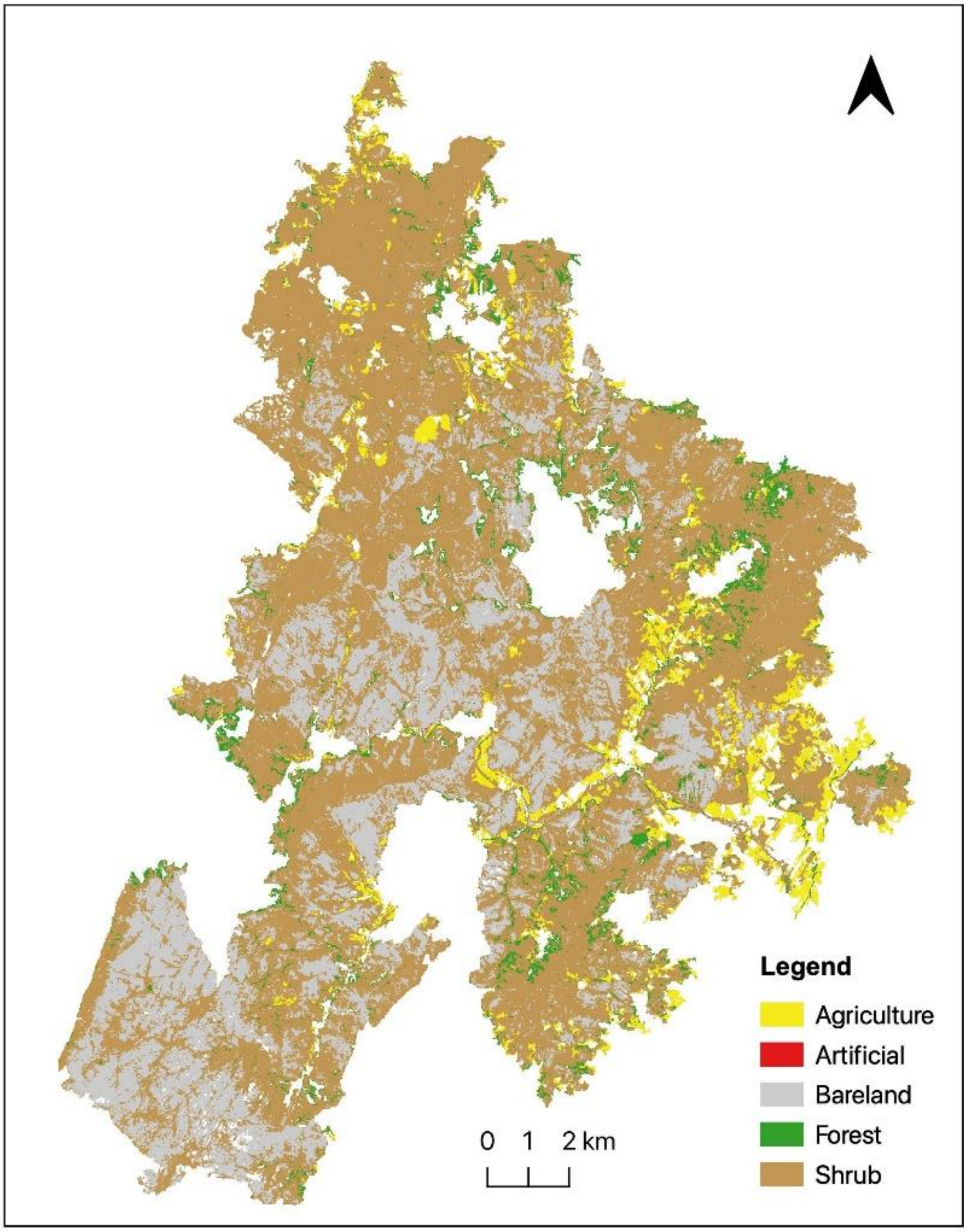

Figure 12. COSc 2023.

Table 19. Analysis of the land cover size in summer 2023 for each model and COSc 2023.

Area(ha)	Agriculture	Artificial	Bareland	Forest	Shrub
COSc 2023	1479.32	5.78	5820.55	1168.25	15757.47
RF_OBIA_S23	6867.58	349.50	10425.99	2316.96	4276.57
RF_PBIA_S23	10254.29	187.83	8555.31	1892.89	3342.48
SVM_OBIA_S23	9822.13	1041.57	9404.46	2196.01	1771.86
SVM_PBIA_S23	14189.20	472.56	7944.88	752.46	876.15

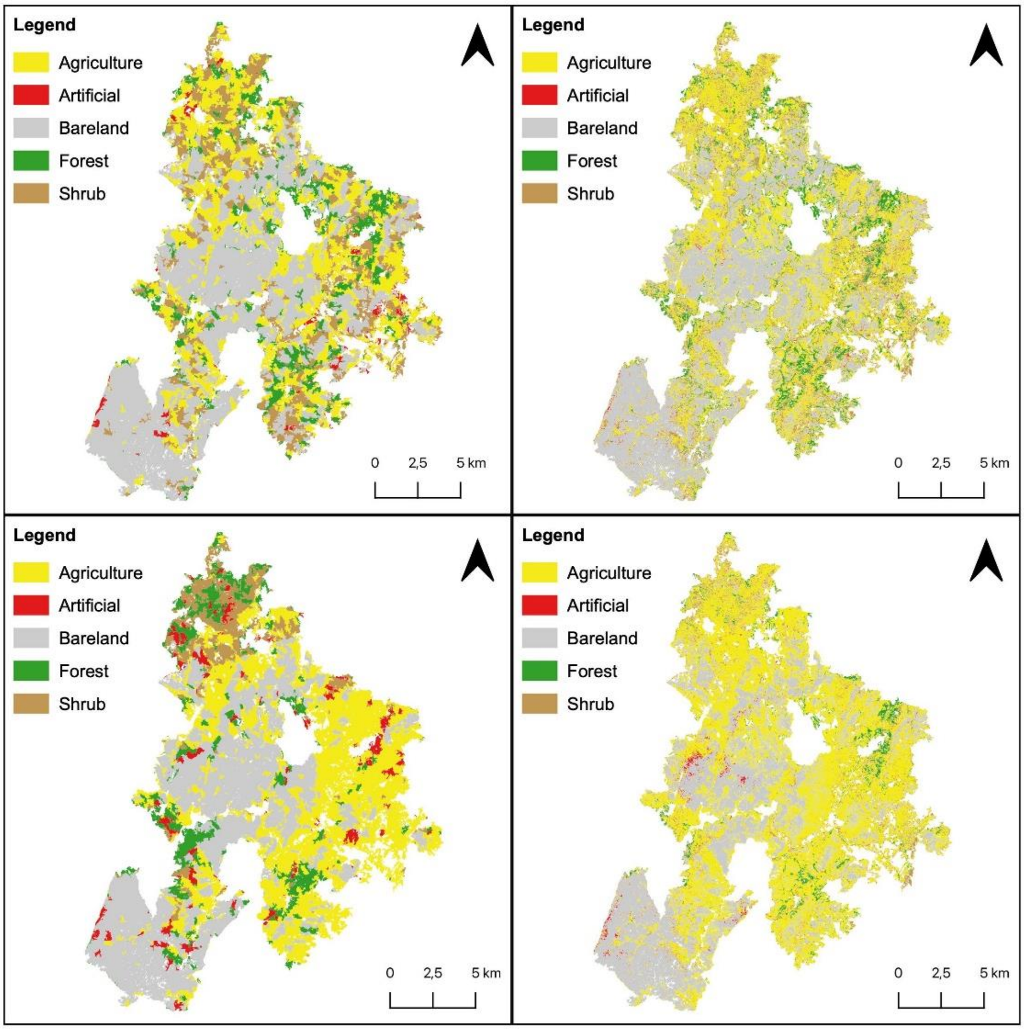

Figure 13. Comparison of land cover maps classified by different models (top left: RF x OBIA, top right: RF x PBIA, bottom left: SVM x OBIA, top left: SVM x PBIA) for summer 2023.

6.4.Post-Wildfire Land Cover Change Detection

Following the results in sub-chapters 6.2 and 6.3, where the RF x OBIA model indicated the highest accuracy in all events among the models while the SVM x PBIA model reflected better visual accuracy against the NDVI map and COSc 2023, land cover change detection was observed for both models. Fig. 14 and 15 present the land cover change in pattern symbols and the unchanged land cover in filled colors. The map on the left in both figures detected a major land cover change to bare land after the 2022 wildfire. As presented in Tables 20 and 21, all the land cover classes had major changes to bare land, which was ecologically reasonable after 98% of the study area was burned in the wildfire event. According to the land cover change detected by the RF x OBIA model (Fig. 14), 75.98% of the land cover changed to bare land post-wildfire, where the paramount area was originally forest that formed 65.38% of the study area (Table 20). In consequence, 84.63% of the study area was covered by bare land after the 2022 wildfire. The map on the right (Fig. 14) shows that a significant size of the study area remained bare land (41.11%, Table 20) in summer 2023. While most of the land cover remained, there was remarkable regeneration of agricultural land, forest, and shrubland; particularly in the north and east of the study area, as shown in Fig. 14. As for land cover change detected by SVM x PBIA model (Fig. 15), 67.94% of the land cover changed to bare land after the 2022 wildfire, making up 71.56% of bare land in the study area, of which forest was originally 46.92% of the study area (Table 21). Furthermore, greater burned area recovery was noticed from the land cover change map of summer 2023 in Fig. 15. It demonstrates a major agricultural land regeneration and a minor forest and shrubland regeneration. Table 21 detailed the major agricultural regeneration from each land cover class, particularly 38.59% of the study area was recovered from bare land to agricultural land, except for forest.

Table 20. The major land cover change of each land cover class from pre-fire 2022 to post-fire 2022, and from post-fire 2022 to summer 2023 [RF x OBIA model].

Major change from	Prefire 2022 to Postfire 2022			Postfire 2022 to Summer 2023		
	To	Area (ha)	%	To	Area (ha)	%
Agriculture	Bareland	1593.07	6.57	Agriculture	690.74	2.85
Artificial	Bareland	70.53	0.29	Artificial	58.79	0.24
Bareland	Bareland	2094.21	8.64	Bareland	9965.35	41.11
Forest	Bareland	15847.11	65.38	Forest	653.9	2.7
Shrub	Bareland	907.34	3.74	Agriculture	302.43	1.25

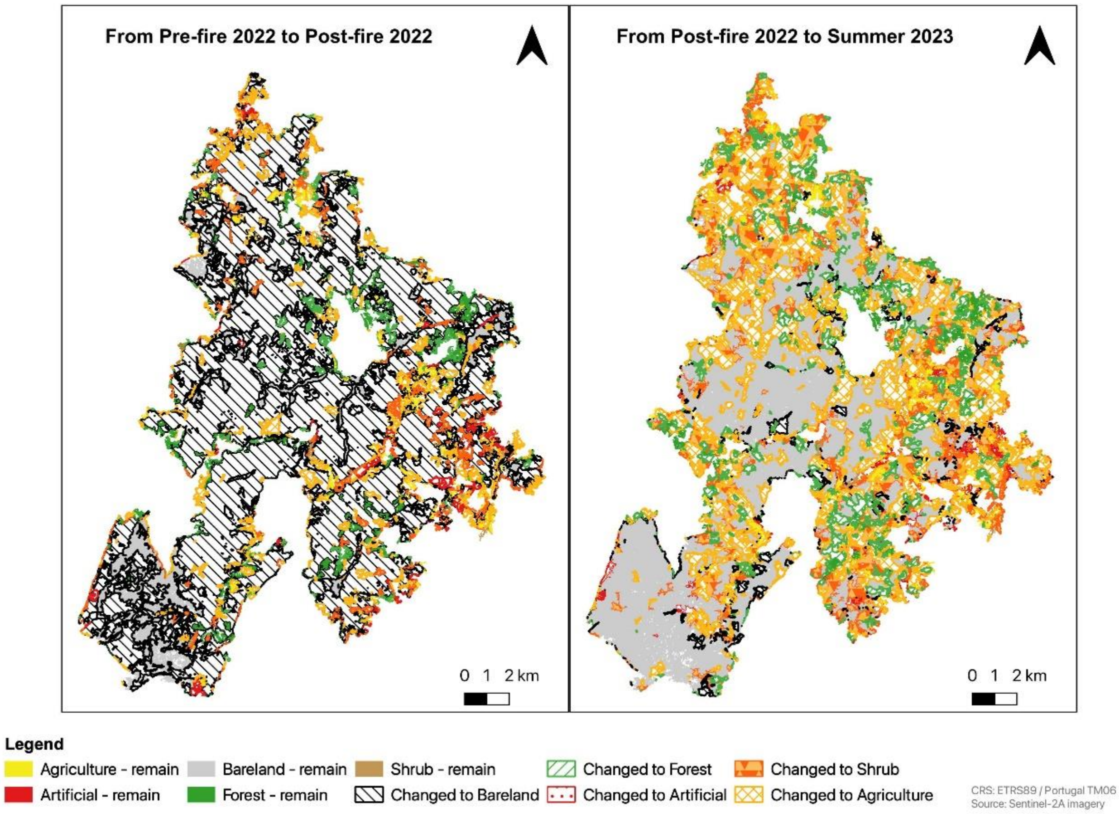

Figure 14. Land cover change detection using RF x OBIA model: pre-wildfire vs. post-wildfire 2022 (left) and post-wildfire 2022 vs. summer 2023 (right).

Table 21. The major land cover change of each land cover class from pre-fire 2022 to post-fire 2022, and from post-fire 2022 to summer 2023 [SVM x PBIA model].

Major change from	Prefire 2022 to Postfire 2022			Postfire 2022 to Summer 2023		
	To	Area (ha)	%	To	Area (ha)	%
Agriculture	Bareland	3305.88	13.64	Agriculture	3881.37	16.01
Artificial	Bareland	28.07	0.12	Agriculture	370.35	1.53
Bareland	Bareland	877.69	3.62	Agriculture	9354.4	38.59
Forest	Bareland	11373.65	46.92	Forest	243.37	1
Shrub	Bareland	1760.7	7.26	Agriculture	450.55	1.9

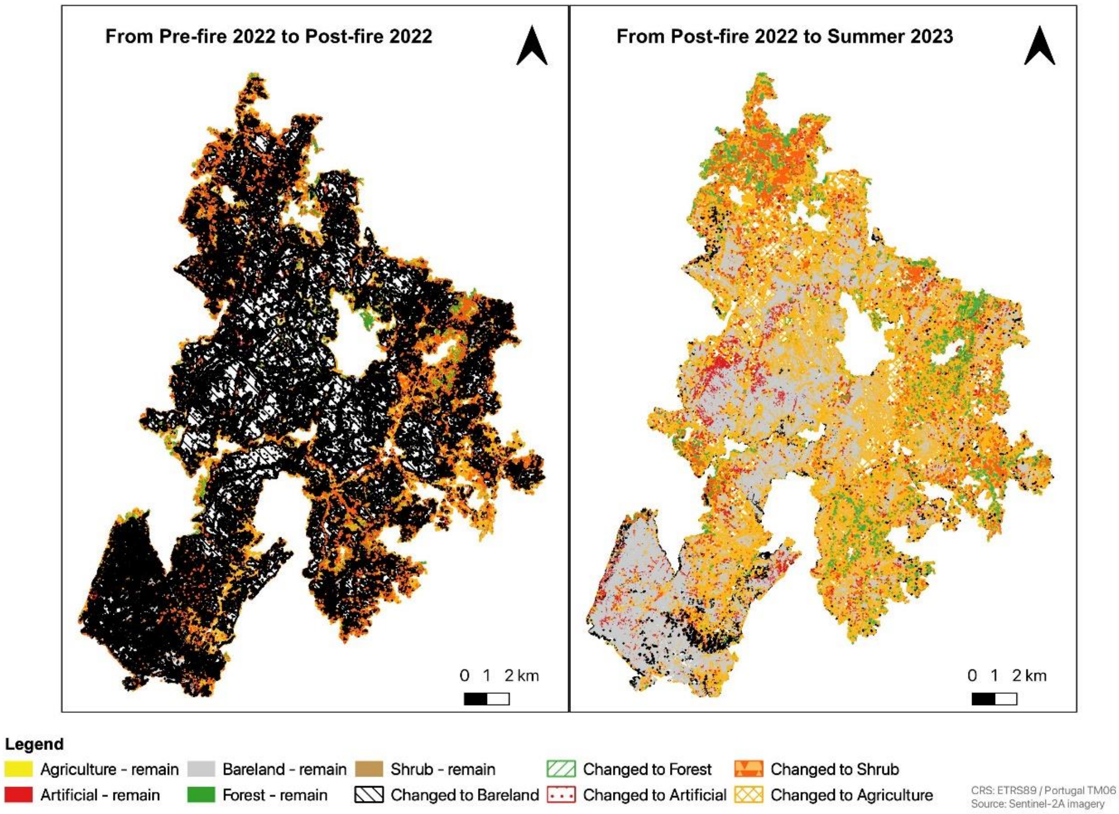

Figure 15. Land cover change detection using SVM x PBIA model: pre-wildfire vs. post-wildfire 2022 (left) and post-wildfire 2022 vs. summer 2023 (right).

6.5.Land Cover Maps

6.5.1.Land Cover Maps – RF x OBIA Model

Fig. 16 presents the land cover maps classified by the RF x OBIA model for the three events. The land cover change is visually noticeable throughout the events. As shown in Table 22, the study area was predominantly covered by forest (73.64%) with a considerable size of bare land (9.31%) in the southwest area, while agricultural land (10.12%) and shrubland (6.22%) spread across the study area before the wildfire. As a consequence of the 2022 wildfire, the study area attained 84.63% of bare land, resulting in minor vegetation of agricultural land (6.83%), forest (4.76%), and shrubland (2.99%) as presented in Table 22. Nearly half of the bare land in the post-wildfire event was recovered in the summer of 2023. Regeneration of vegetation was reflected in the land cover change: agricultural land (28.34%), shrubland (17.65%), and forest (9.56%). The recovery was noticeable across the study area in the summer of 2023. Moreover, the artificial area remained the smallest (not more than 1.44%, Table 22) land cover within the study area. Furthermore, forest and shrubland were observed to be vulnerable to wildfire, with 93.54% and 51.93% of their land cover burned in the 2022 wildfires, respectively (Table 22). On the other hand, agricultural land was more fire resistant, with 32.5% of its land cover burned in the wildfire event.

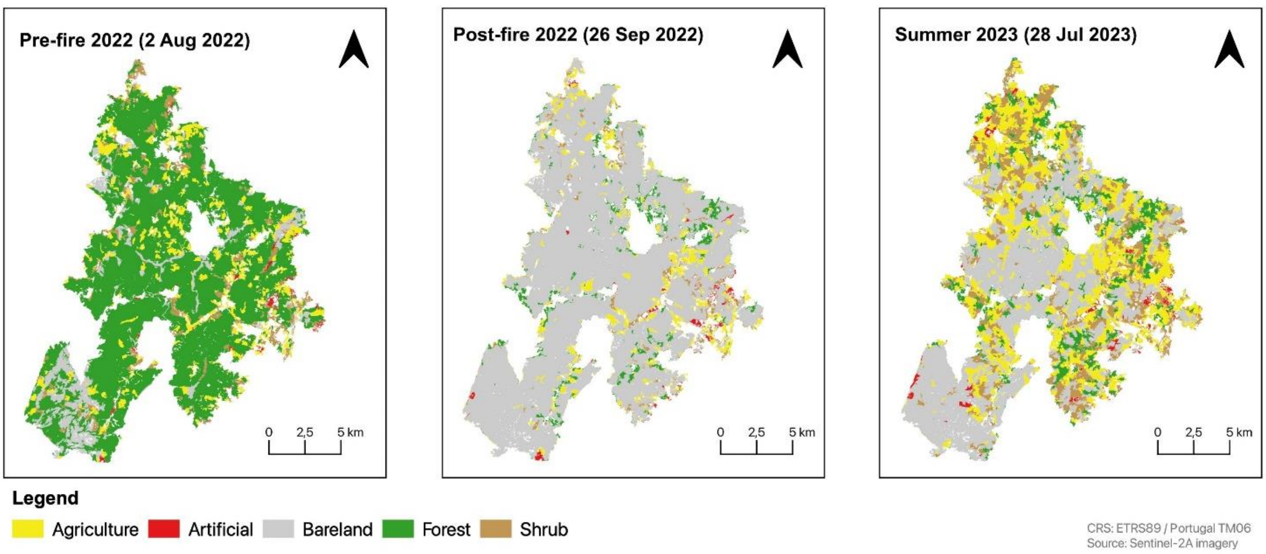

Figure 16. The land cover maps classified using RF x OBIA model.

Table 22. Land Cover Changes: Prefire 2022, Postfire 2022, and Summer 2023 [RF x OBIA].

ID	Land Cover	Prefire 2022		Postfire 2022		Summer 2023	
		Area (ha)	%	Area (ha)	%	Area (ha)	%
0	Agriculture	2452.94	10.12	1655.68	6.83	6867.58	28.34
1	Artificial	173.57	0.72	191.49	0.79	349.5	1.44
2	Bareland	2256.58	9.31	20512.27	84.63	10425.99	43.02
3	Forest	17846.92	73.64	1152.91	4.76	2316.96	9.56
4	Shrub	1506.59	6.22	724.23	2.99	4276.57	17.65
	Total	24236.6	100	24236.6	100	24236.6	100

6.5.2.Land Cover Maps – SVM x PBIA Model

Fig. 17 presents the land cover maps classified by the SVM x PBIA model for the three events. The land cover change is visually noticeable throughout the events. Fig. 17 indicates that the land cover map before the wildfire (left) reflected the study area was majorly covered with vegetation: forest (61.41%), agricultural land (21.83%) and shrubland (12.42%), where bare land (4.06%) and artificial land (0.26%) occupied less than 5% of the study area (Table 23). As a consequence of the 2022 wildfire, the study area attained 71.56% of bare land, which burned 97.37% and 75.65% of forest and shrubland, respectively (Table 23). This has again proved the vulnerability of forests and shrubland against wildfire. On the other hand, agricultural land was more fire resistant, with 97.73% of its land cover preserved in the wildfire event. More than half of the bare land was recovered in the summer of 2023; major agricultural regeneration was noticed where agricultural land occupied 58.55% of the study area while forest (3.1%) had a smaller occupation than shrubland (3.62%) in the summer of 2023 (Table 23). Furthermore, the artificial area remained the smallest (not more than 2.5%, Table 23) land cover within the study area.

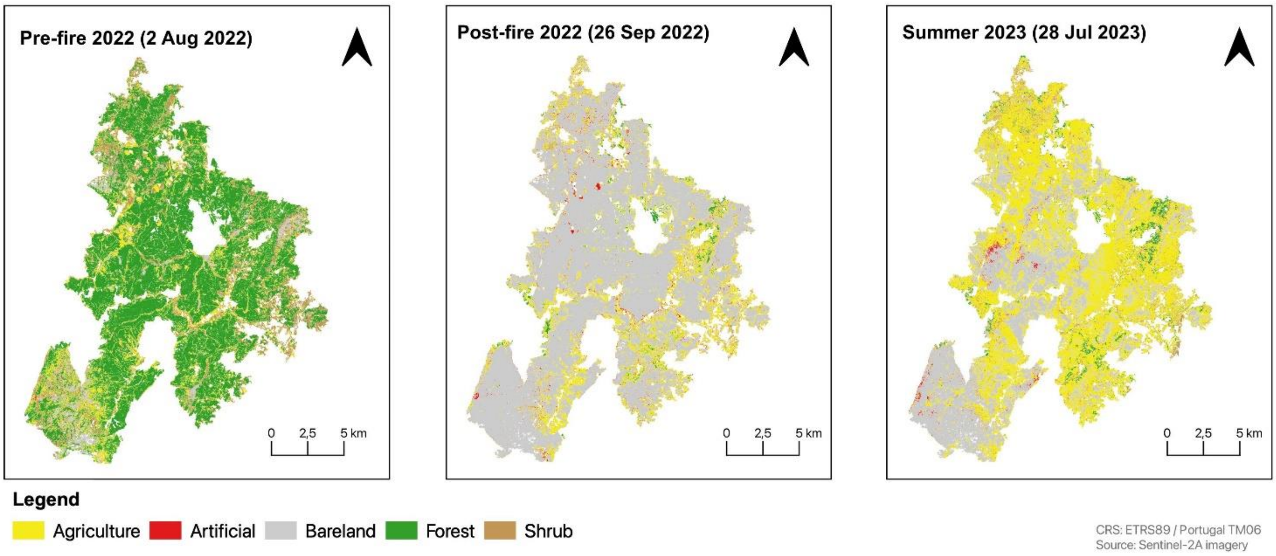

Figure 17. The land cover maps classified using SVM x PBIA model.

Table 23. Land Cover Changes: Prefire 2022, Postfire 2022, and Summer 2023 [SVM x PBIA].

ID	Land Cover	Prefire 2022		Postfire 2022		Summer 2023	
		Area (ha)	%	Area (ha)	%	Area (ha)	%
0	Agriculture	5292.29	21.83	5,172.30	21.34	14189.20	58.55
1	Artificial	63.35	0.26	593.50	2.45	472.56	1.95
2	Bareland	984.99	4.06	17,346.21	71.56	7944.88	32.78
3	Forest	14884.9	61.41	391,02	1.61	752.46	3.1
4	Shrub	3010.71	12.42	733.09	3.02	876.15	3.62
	Total	24236.24	100	24236.12	100	24235.25	100

6.5.3.Conclusion

In pre-wildfire events, the RF x OBIA model indicated larger forest and bare land areas, while the SVM x PBIA model indicated larger agricultural and shrubland areas compared to each other. In addition, the RF x OBIA model demonstrated a larger bare land while the SVM x PBIA model showed slightly smaller bare land with higher preservation of agricultural land in the post-wildfire events. Both models confirmed the vulnerability of forest and shrubland against wildfire and proven the fire resistance of agricultural land. Furthermore, the SVM x PBIA model detailed a larger burned area recovery with major agricultural regeneration, while the RF x OBIA model demonstrated a smaller burned area recovery with the regeneration of agricultural land, shrubland, and forest in summer 2023.

7. Discussion

In this research, two LULC classification approaches, OBIA and PBIA, were integrated with RF and SVM classifiers, using GEE to optimize the land cover classification for the study area. Kappa coefficient was interpreted as an improvement upon OA [72]. RF classifier achieved almost perfect agreement of kappa results with both OBIA and PBIA approaches. Unlike the RF classifier, the SVM classifier had relatively unstable performance, and the kappa results ranged from substantial to almost perfect agreement [72]. Referring to Fig. 9, OBIA and PBIA approaches were individually presented with similar F1 score rankings for both RF and SVM classifiers in each event. Hence, choosing the right classifier is vital to increase the accuracy of land cover classification. Furthermore, **4. Shrub**, the land cover class with the lowest F1 score in most events, was always misclassified with **0. Agriculture** had a lower F1 score as well. It is challenging to classify vegetation as they have very similar spectral reflectance [47, 73, 74]. According to the metric results, the RF x OBIA model achieved the highest accuracy, while the SVM models had lower accuracy for land cover classification in all events.

In contrast, to the metric results, comparison with NDVI map, the dNBR map, and COSc 2023 showed a completely different finding. SVM x PBIA model which had lower value of evaluation metrics, demonstrates a more analogous visual result among the land cover maps. The pre-wildfire map classified by the SVM x PBIA model (Fig. 11) corresponded to the NDVI map (Fig. 7) of the same event. This is logical as the NDVI map was produced by pixels comparison of the NIR band and red band, even the RF x PBIA map had better visual results than the RF x OBIA map (Fig. 11). As for the comparison between dNBR and post-wildfire land cover maps, RF x OBIA map had largest bare land among all the pre-wildfire maps (Table 17), and the bare land size was between the burned area classified by MLC and USGS for moderate to high five severity (Fig. 6). Nevertheless, a smaller bare land size classified by SVM x PBIA model was due to larger agricultural land in the study area, and which was proven to be more fire resistant. Thus, BA22 and dNBR were inadequate to compare the accuracy of post-wildfire land cover maps. Pertaining to the comparison of COSs 2023 with land cover maps of summer 2023, the SVM x PBIA map closely resembled COSc 2023, except the major shrubland area in COSc 2023 was classified as agricultural land on the map. There are a few limitations to this accuracy validation. First, both maps are not comparable as the land cover map generated in this research was based on a specific date while the land cover classification in COSc 2023 was based on the monthly mean of a year as noted in sub-chapter 5.6.7.. Moreover, there is no ground truth data to validate whether the agricultural land on the SVM x PBIA map was presented correctly and whether the shrubland presented on COSc 2023 indicated the vegetation dynamic after the agricultural harvest. Furthermore, whether it was the failure of SVM x PBIA model in distinguishing shrubland and agricultural land that caused the difference of the land cover was also untestable. Overall, the NDVI map, dNBR map, and COSc 2023 were not the most adequate to serve as a solid comparison to examine the accuracy of the land cover maps.

7.1. Accuracy of RF & SVM in Monitoring Burned Area Recovery

On account of no ground truth data or solid comparison is available, both RF and SVM classifiers are not justified to be reliable for monitoring the burned area recovery in the study area even though RF x OBIA maps indicated a high value of evaluation metrics, and SVM x PBIA maps are visually accurate compared to NDVI map and COSc 2023. The output produced by both models were significantly different, it is arguable which model is more accurate for reference.

7.2.Comparison of OBIA and PBIA for Land Cover Classification in the Study Area

OBIA and PBIA approaches had difficulties in classifying shrubland in all events, particularly with the SVM x PBIA model. In the RF x OBIA model, the accuracy for shrubland classification was still relatively high where the F1 score was above 0.91 in all events. The slight misclassification between artificial land and shrubland might be due to the characteristics of SNIC considering the neighbouring spatial feature, while sparse vegetation around the artificial land was common in the study area. In this regard, the parameter setting for SNIC is crucial. Lower scale is computationally expensive for large areas, and it is unnecessary for large-scale homogeneous landscapes in the study area. The balance in determining an optimal distance unit among the land cover classes is critical. Regardless of the high accuracy examined by the evaluation metrics, the difference between the land cover maps and COSc 2023 was not assessable due to the inequivalence of the dataset.

In addition, shrubland and agricultural land were always misclassified interchangeably in all models with the PBIA approach. Furthermore, the SVM classifier was unable to classify agricultural land precisely with both OBIA and PBIA approaches for the study area. The challenge of classifying the vegetation accurately remains a major concern as there are three (3) classes of vegetation in this research, and the capacity to classify the vegetation at lower levels is an asset to observing the vegetation dynamics and the recovery of biodiversity in the study area.

8. Conclusions

8.1.Conclusions

This research aims to identify the best model for land cover classification of the study area using GEE. A land cover map provides important information for emergency planning and disaster management during a wildfire and burned area and vegetation monitoring after a wildfire. As official data is commonly available at longer intervals, RS application and ML algorithms were utilized in many studies to conduct periodic assessments for post-wildfire recovery process management [41], land cover assessment after wildfire [49], and post-wildfire land cover change detection [46]. In Portugal, the SNIG produces the LULC map annually. To complement this shortcoming, Sentinel-2A imagery was utilized, to process with two LULC classification approaches, OBIA and PBIA. The feature collections were subsequently trained with RF and SVM classifiers on GEE. There were four (4) models: RF x OBIA, RF x PBIA, SVM x OBIA, and SVM x PBIA, trained for the dataset of each event. The land cover classification was further assessed with evaluation metrics: (a) confusion matrix, (b) F1 score, (c) OA, and (d) kappa coefficient. In addition, the land cover maps were compared with NDVI map, BA22, dNBR map, and COSc 2023. The evaluation metric results were very consistent; the RF x OBIA model was the most accurate for land cover classification in the study area, while comparison with NDVI map and COSc 2023 indicated that SVM x PBIA map resembled the maps better. However, the validation of land cover maps against COSc 2023 was not ideal as the land cover map generated in this research was based on a specific date, while the land cover classification in COSc 2023 was based on the monthly mean of a year, as noted in the sub-chapter 5.6.7. In addition, there is no access to field data which is available for validation purposes. Considering these limitations, the best model for land cover classification of the study area was not conclusively determined. Nonetheless, this research provided some important insights:

(a) The land cover classification with the highest values of evaluation metrics might not reflect the same level of accuracy in map presentation.

(b) Concurrent with Lawrence and Moran's studies [57], more classifiers should be tested to identify the most accurate model.

(c) The PBIA approach had difficulties in distinguishing the vegetation; the OBIA approach tackled this problem better with the RF classifier but not with the SVM classifier.

(d) The SVM classifier had unstable performance where the accuracy in classifying the land cover classes fluctuates in different events.

8.2.Future work

Although the objectives of this research were not met completely, it set the groundwork for future research. In future work, it is ideal to test the model with imagery of other date with available field data, to identify an optimized model to classify the land cover for periodic assessment in the study area. Since the SVM x PBIA model strongly resembled COSc 2023 while achieving low accuracy in evaluation metrics, different parameters can be tested and refined to optimize the result in future works. Furthermore, different ML and deep learning algorithms can be tested to improve the land cover classification result.

References

[1] D. M. Szpakowski and J. L. R. Jensen, "A Review of the Applications of Remote Sensing in Fire Ecology," *Remote Sensing,* vol. 11, no. 22, Nov 2019, Art no. 2638, doi: 10.3390/rs11222638.

[2] M. Bashirzadeh, M. Abedi, R. P. Shefferson, and M. Farzam, "Post-Fire Recovery of Plant Biodiversity Changes Depending on Time Intervals since Last Fire in Semiarid Shrublands," *Fire,* vol. 6, no. 3, p. 103, 2023. [Online]. Available: https://www.mdpi.com/2571-6255/6/3/103.

[3] Eurostat, "Archive:Land cover and land use statistics at regional level," 2014. [Online]. Available: https://ec.europa.eu/eurostat/statistics-explained/index.php?title=Archive:Land_cover_and_land_use_statistics_at_regional_level.

[4] U. S. E. P. Agency, "Land Cover - Environmental Effects," 2023. [Online]. Available: https://www.epa.gov/report-environment/land-cover#:~:text=Land%20cover%20affects%20or%20influences,%2C%20climate%2C%20and%2

0carbon%20storage.

[5] A. Calsamiglia, M. E. Lucas-Borja, J. Fortesa, J. García-Comendador, and J. Estrany, "Changes in Soil Quality and Hydrological Connectivity Caused by the Abandonment of Terraces in a Mediterranean Burned Catchment," *Forests,* vol. 8, no. 9, Sep 2017, Art no. 333, doi: 10.3390/f8090333.

[6] C. Papathanasiou, C. Makropoulos, and M. Mimikou, "Hydrological modelling for flood forecasting: Calibrating the post-fire initial conditions," *Journal of Hydrology,* vol. 529, pp. 1838-1850, Oct 2015, doi: 10.1016/j.jhydrol.2015.07.038.

[7] C. R. Stoof *et al.*, "Soil surface changes increase runoff and erosion risk after a low-moderate severity fire," *Geoderma,* vol. 239, pp. 58-67, Feb 2015, doi: 10.1016/j.geoderma.2014.09.020.

[8] T. Fournier, J. Fèvre, F. Carcaillet, and C. Carcaillet, "For a few years more: reductions in plant diversity 70 years after the last fire in Mediterranean forests," *Plant Ecology,* vol. 221, no. 7, pp. 559-576, Jul 2020, doi: 10.1007/s11258-020-01034-z.

[9] F. Lloret and M. Vilà, "Diversity patterns of plant functional types in relation to fire regime and previous land use in Mediterranean woodlands," *Journal of Vegetation Science,* vol. 14, no. 3, pp. 387-398, Jun 2003, doi: 10.1111/j.1654-1103.2003.tb02164.x.

[10] A. Viana-Soto, A. Okujeni, D. Pflugmacher, M. García, I. Aguado, and P. Hostert, "Quantifying post-fire shifts in woody-vegetation cover composition in Mediterranean pine forests using Landsat time series and regression-based unmixing," *Remote Sensing of Environment,* vol. 281, Nov 2022, Art no. 113239, doi: 10.1016/j.rse.2022.113239.

[11] A. Dolny, S. Ozana, M. Burda, and F. Harabis, "Effects of Landscape Patterns and Their Changes to Species Richness, Species Composition, and the Conservation

Value of Odonates (Insecta)," *Insects,* vol. 12, no. 6, Jun 2021, Art no. 478, doi: 10.3390/insects12060478.

[12] S. S. Hasan, L. Zhen, M. G. Miah, T. Ahamed, and A. Samie, "Impact of land use change on ecosystem services: A review," *Environmental Development,* vol. 34, Jun 2020, Art no. 100527, doi: 10.1016/j.envdev.2020.100527.

[13] Y. F. Wiersma, T. D. Nudds, and D. H. Rivard, "Models to distinguish effects of landscape patterns and human population pressures associated with species loss in Canadian national parks," *Landscape Ecology,* vol. 19, no. 7, pp. 773-786, 2004, doi: 10.1007/s10980-005-3989-y.

[14] A. A. Tahiru, D. A. Doke, and B. N. Baatuuwie, "Effect of land use and land cover changes on water quality in the Nawuni Catchment of the White Volta Basin, Northern Region, Ghana," *Applied Water Science,* vol. 10, no. 8, Jul 2020, Art no. 198, doi: 10.1007/s13201-020-01272-6.

[15] D. N. Wear, M. G. Turner, and R. J. Naiman, "Land cover along an urban-rural gradient: Implications for water quality," *Ecological Applications,* vol. 8, no. 3, pp. 619-630, Aug 1998, doi: 10.2307/2641254.

[16] C. Wilson and Q. Weng, "Assessing Surface Water Quality and Its Relation with Urban Land Cover Changes in the Lake Calumet Area, Greater Chicago," *Environmental Management,* vol. 45, no. 5, pp. 1096-1111, 2010/05/01 2010, doi: 10.1007/s00267-010-9482-6.

[17] R. Alkama and A. Cescatti, "Biophysical climate impacts of recent changes in global forest cover," *Science,* vol. 351, no. 6273, pp. 600-604, Feb 2016, doi: 10.1126/science.aac8083.

[18] J. J. Feddema *et al.*, "The importance of land-cover change in simulating future climates," *Science,* vol. 310, no. 5754, pp. 1674-1678, Dec 2005, doi: 10.1126/science.1118160.

[19] K. C. Seto, M. Fragkias, B. Güneralp, and M. K. Reilly, "A Meta-Analysis of Global Urban Land Expansion," *Plos One,* vol. 6, no. 8, Aug 2011, Art no. e23777, doi: 10.1371/journal.pone.0023777.

[20] R. A. Houghton *et al.*, "Carbon emissions from land use and land-cover change," *Biogeosciences,* vol. 9, no. 12, pp. 5125-5142, 2012, doi: 10.5194/bg-9-5125-2012.

[21] M. Zhao and A. J. Pitman, "The impact of land cover change and increasing carbon dioxide on the extreme and frequency of maximum temperature and convective precipitation," *Geophysical Research Letters,* vol. 29, no. 6, pp. 2-1-2-4, 2002.

[22] J. R. C. J. European Commission. "Monitoring areas damaged by forest fires in Serra da Estrela, Portugal (2023-05-02)." European Commission, Joint Research Centre (JRC). http://data.europa.eu/89h/9433731c-2c95-4588-b5fe-979d04633c29 (accessed 13.6.2024.

[23] E. Copernicus. "EFFIS Estimates for European Union." https://effis.jrc.ec.europa.eu/apps/effis.statistics/estimates/EU/2024/2006/2023 (accessed.

[24] M. Turco *et al.*, "Climate drivers of the 2017 devastating fires in Portugal," *Scientific Reports,* vol. 9, no. 1, p. 13886, 2019/10/10 2019, doi: 10.1038/s41598-019-50281-2.

[25] M. Holroyd. "Eleven people acquitted of negligence over deadly 2017 wildfires in Portugal." Euronews. https://www.euronews.com/2022/09/13/eleven-people-acquitted-of-negligence-over-

deadly-2017-wildfires-in-portugal (accessed.

[26] M. Lusa, "August fire was the biggest in 47 years in Serra da Estrela," ed: Diário de Notícias, 2022.

[27] (2024). *Burned territories - burned area 2022*. [Online] Available: https://sig.icnf.pt/portal/home/item.html?id=983c4e6c4d5b4666b258a3ad5f3ea5af

[28] Natural.PT. "Serra da Estrela Natural Park." https://natural.pt/protected-areas/parque-

natural-serra-estrela?locale=pt (accessed.

[29] G. Aziz, N. Minallah, A. Saeed, J. Frnda, and W. Khan, "Remote sensing based forest cover classification using machine learning," *Scientific Reports,* vol. 14, no. 1, p. 69, 2024/01/02 2024, doi: 10.1038/s41598-023-50863-1.

[30] V. F. Rodriguez-Galiano, B. Ghimire, J. Rogan, M. Chica-Olmo, and J. P. Rigol-Sanchez, "An assessment of the effectiveness of a random forest classifier for land-cover classification," *ISPRS Journal of Photogrammetry and Remote Sensing,* vol. 67, pp. 93-104, 2012/01/01/ 2012, doi: https://doi.org/10.1016/j.isprsjprs.2011.11.002.

[31] X. Huang and J. R. Jensen, "A machine-learning approach to automated knowledge-base building for remote sensing image analysis with GIS data," *Photogrammetric engineering and remote sensing,* vol. 63, no. 10, pp. 1185-1193, 1997.

[32] A. E. Maxwell, T. A. Warner, and F. Fang, "Implementation of machine-learning classification in remote sensing: an applied review," *International Journal of Remote Sensing,* vol. 39, no. 9, pp. 2784-2817, 2018/05/03 2018, doi: 10.1080/01431161.2018.1433343.

[33] B. B. Shrestha, "Approach for Analysis of Land-Cover Changes and Their Impact on Flooding Regime," *Quaternary,* vol. 2, no. 3, p. 27, 2019. [Online]. Available: https://www.mdpi.com/2571-550X/2/3/27.

[34] F. Githui, F. Mutua, and W. Bauwens, "Estimating the impacts of land-cover change on runoff using the soil and water assessment tool (SWAT): case study of Nzoia catchment, Kenya / Estimation des impacts du changement d'occupation du sol sur l'écoulement à l'aide de SWAT: étude du cas du bassin de Nzoia, Kenya," *Hydrological Sciences Journal,* vol. 54, no. 5, pp. 899-908, 2009/10/01 2009, doi: 10.1623/hysj.54.5.899.

[35] S. Wu *et al.*, "Global patterns and influencing factors of post-fire land cover change," *Global and Planetary Change,* vol. 223, p. 104076, 2023/04/01/ 2023, doi: https://doi.org/10.1016/j.gloplacha.2023.104076.

[36] B. Klobucar, N. Sang, and T. B. Randrup, "Comparing ground and remotely sensed measurements of urban tree canopy in private residential property," *Trees, Forests and People,* vol. 5, p. 100114, 2021.

[37] F. Pérez-Cabello, R. Montorio, and D. B. Alves, "Remote sensing techniques to assess post-fire vegetation recovery," *Current Opinion in Environmental Science & Health,* vol. 21, p. 100251, 2021/06/01/ 2021, doi: https://doi.org/10.1016/j.coesh.2021.100251.

[38] J.-H. Ryu, K.-S. Han, S. Hong, N.-W. Park, Y.-W. Lee, and J. Cho, "Satellite-Based Evaluation of the Post-Fire Recovery Process from the Worst Forest Fire Case in South Korea," *Remote Sensing,* vol. 10, no. 6, p. 918, 2018. [Online]. Available: https://www.mdpi.com/2072-4292/10/6/918.

[39] A. Ghorbanian, M. Kakooei, M. Amani, S. Mahdavi, A. Mohammadzadeh, and M. Hasanlou, "Improved land cover map of Iran using Sentinel imagery within Google Earth Engine and a novel automatic workflow for land cover classification using migrated training samples," *ISPRS Journal of Photogrammetry and Remote Sensing,* vol. 167, pp. 276-288, 2020/09/01/ 2020, doi: https://doi.org/10.1016/j.isprsjprs.2020.07.013.

[40] M. Hesping, "Remote sensing-based land cover classification and change detection using Sentinel-2 data and Random Forest: A case study of Rusinga Island, Kenya," ed, 2020.

[41] V. Lebourgeois, S. Dupuy, É. Vintrou, M. Ameline, S. Butler, and A. Bégué, "A Combined Random Forest and OBIA Classification Scheme for Mapping Smallholder Agriculture at Different Nomenclature Levels Using Multisource Data (Simulated Sentinel-2 Time Series, VHRS and DEM)," *Remote Sensing,* vol. 9, no. 3, p. 259, 2017. [Online]. Available: https://www.mdpi.com/2072-4292/9/3/259.

[42] S. T. Seydi, M. Akhoondzadeh, M. Amani, and S. Mahdavi, "Wildfire Damage Assessment over Australia Using Sentinel-2 Imagery and MODIS Land Cover Product within the Google Earth Engine Cloud Platform," *Remote Sensing,* vol. 13, no. 2, p. 220, 2021. [Online]. Available: https://www.mdpi.com/2072-4292/13/2/220.

[43] J. Xiong *et al.*, "Nominal 30-m Cropland Extent Map of Continental Africa by Integrating Pixel-Based and Object-Based Algorithms Using Sentinel-2 and Landsat-8 Data on Google Earth Engine," *Remote Sensing,* vol. 9, no. 10, p. 1065, 2017. [Online]. Available: https://www.mdpi.com/2072-4292/9/10/1065.

[44] G. M. Foody, N. Campbell, N. Trodd, and T. Wood, "Derivation and applications of probabilistic measures of class membership from the maximum-likelihood classification," *Photogrammetric engineering and remote sensing,* vol. 58, no. 9, pp. 1335-1341, 1992.

[45] G. Lazzeri, W. Frodella, G. Rossi, and S. Moretti, "Multitemporal Mapping of Post-Fire Land Cover Using Multiplatform PRISMA Hyperspectral and Sentinel-UAV Multispectral Data: Insights from Case Studies in Portugal and Italy," *Sensors,* vol. 21, no. 12, p. 3982, 2021. [Online]. Available: https://www.mdpi.com/1424-8220/21/12/3982.

[46] R. Lasaponara, N. Abate, C. Fattore, A. Aromando, G. Cardettini, and M. Di Fonzo, "On the Use of Sentinel-2 NDVI Time Series and Google Earth Engine to Detect Land-Use/Land-Cover Changes in Fire-Affected Areas," *Remote Sensing,* vol. 14, no. 19, p. 4723, 2022. [Online]. Available: https://www.mdpi.com/2072-4292/14/19/4723.

[47] I. C. L. B. DE OLIVEIRA, "REMOTE SENSING FOR LAND USE/LAND COVER MAPPING IN ALMADA," 2022.

[48] L. Martinez-Sanchez *et al.*, "Automatic classification of land cover from LUCAS in-situ landscape photos using semantic segmentation and a Random Forest model," *Environmental Modelling & Software,* vol. 172, p. 105931, 2024/01/01/ 2024, doi: https://doi.org/10.1016/j.envsoft.2023.105931.

[49] L. C. Chen, G. Papandreou, I. Kokkinos, K. Murphy, and A. L. Yuille, "DeepLab: Semantic Image Segmentation with Deep Convolutional Nets, Atrous Convolution, and Fully Connected CRFs," *IEEE Transactions on Pattern Analysis and Machine Intelligence,* vol. 40, no. 4, pp. 834-848, 2018, doi: 10.1109/TPAMI.2017.2699184.

[50] J. Guo *et al.*, "Gluoncv and gluonnlp: Deep learning in computer vision and natural language processing," *Journal of Machine Learning Research,* vol. 21, no. 23, pp. 1-7, 2020.

[51] B. Zhou *et al.*, "Semantic understanding of scenes through the ade20k dataset," *International Journal of Computer Vision,* vol. 127, pp. 302-321, 2019.

[52] A. E. Maxwell, T. A. Warner, M. P. Strager, J. F. Conley, and A. L. Sharp, "Assessing machine-learning algorithms and image- and lidar-derived variables for GEOBIA classification of mining and mine reclamation," *International Journal of Remote Sensing,* vol. 36, no. 4, pp. 954-978, 2015/02/16 2015, doi: 10.1080/01431161.2014.1001086.

[53] P. Thanh Noi and M. Kappas, "Comparison of Random Forest, k-Nearest Neighbor, and Support Vector Machine Classifiers for Land Cover Classification Using Sentinel-2 Imagery," *Sensors,* vol. 18, no. 1, p. 18, 2018. [Online]. Available: https://www.mdpi.com/1424-8220/18/1/18.

[54] C. Zhang and Z. Xie, "Object-based Vegetation Mapping in the Kissimmee River Watershed Using HyMap Data and Machine Learning Techniques," *Wetlands,* vol. 33, no. 2, pp. 233-244, 2013/04/01 2013, doi: 10.1007/s13157-012-0373-x.

[55] A. E. Maxwell, M. P. Strager, T. A. Warner, N. P. Zégre, and C. B. Yuill, "Comparison of NAIP orthophotography and RapidEye satellite imagery for mapping of mining and mine reclamation," *GIScience & Remote Sensing,* vol. 51, no. 3, pp. 301-320, 2014/05/04 2014, doi: 10.1080/15481603.2014.912874.

[56] R. Saini and S. Rawat, "Land use land cover classification in remote sensing using machine learning techniques," in *2023 1st International Conference on Innovations in High Speed Communication and Signal Processing (IHCSP)*, 2023: IEEE, pp. 99-104.

[57] R. L. Lawrence and C. J. Moran, "The AmericaView classification methods accuracy comparison project: A rigorous approach for model selection," *Remote Sensing of Environment,* vol. 170, pp. 115-120, 2015/12/01/ 2015, doi: https://doi.org/10.1016/j.rse.2015.09.008.

[58] D. Shi and X. Yang, "Support Vector Machines for Land Cover Mapping from Remote Sensor Imagery," 2015, pp. 265-279.

[59] J. Cervantes, F. García Lamont, A. López-Chau, L. Rodríguez Mazahua, and J. Sergio Ruíz, "Data selection based on decision tree for SVM classification on large data sets," *Applied Soft Computing,* vol. 37, pp. 787-798, 2015/12/01/ 2015, doi: https://doi.org/10.1016/j.asoc.2015.08.048.

[60] J. Cervantes, X. Li, W. Yu, and K. Li, "Support vector machine classification for large data sets via minimum enclosing ball clustering," *Neurocomputing,* vol. 71, no. 4, pp. 611-619, 2008/01/01/ 2008, doi: https://doi.org/10.1016/j.neucom.2007.07.028.

[61] M. D. Hossain and D. Chen, "Segmentation for Object-Based Image Analysis (OBIA): A review of algorithms and challenges from remote sensing perspective," *ISPRS Journal of Photogrammetry and Remote Sensing,* vol. 150, pp. 115-134, 2019/04/01/ 2019, doi: https://doi.org/10.1016/j.isprsjprs.2019.02.009.

[62] VisitPortugal. "Serra da Estrela." https://www.visitportugal.com/en/destinos/centro-de-portugal/73759 (accessed 13.11.2023.

[63] Life-Relict. "Special Area of Conservation of Estrela Mountain." http://www.liferelict.ect.uevora.pt/index.php/areas-de-intervencao/?lang=en (accessed 13.11.2023.

[64] G. Estrela. "Estrela Geopark." https://www.geoparkestrela.pt/menu (accessed.

[65] G. E. Engine. "FAQ." https://earthengine.google.com/faq/ (accessed.

[66] A. Teodoro and A. Amaral, "A Statistical and Spatial Analysis of Portuguese Forest Fires in Summer 2016 Considering Landsat 8 and Sentinel 2A Data," *Environments,* vol. 6, no. 3, p. 36, 2019. [Online]. Available: https://www.mdpi.com/2076-3298/6/3/36.

[67] L. Ma, M. C. Li, X. X. Ma, L. Cheng, P. J. Du, and Y. X. Liu, "A review of supervised object-based land-cover image classification," *Isprs Journal of Photogrammetry and Remote Sensing,* vol. 130, pp. 277-293, Aug 2017, doi: 10.1016/j.isprsjprs.2017.06.001.

[68] R. Goldblatt, W. You, G. Hanson, and A. K. Khandelwal, "Detecting the Boundaries of Urban Areas in India: A Dataset for Pixel-Based Image Classification in Google Earth Engine," *Remote Sensing,* vol. 8, no. 8, Aug 2016, Art no. 634, doi: 10.3390/rs8080634.

[69] A. Tassi, D. Gigante, G. Modica, L. Di Martino, and M. Vizzari, "Pixel- vs. Object-Based Landsat 8 Data Classification in Google Earth Engine Using Random Forest: The Case Study of Maiella National Park," *Remote Sensing,* vol. 13, no. 12, Jun 2021, Art no. 2299, doi: 10.3390/rs13122299.

[70] G. E. Engine. "Reference." https://developers.google.com/earth-engine/apidocs/ee-algorithms-image-segmentation-snic (accessed 3.6.2024.

[71] S. Yousefi *et al.*, "Image Classification and Land Cover Mapping Using Sentinel-2 Imagery: Optimization of SVM Parameters," *Land,* vol. 11, no. 7, Jul 2022, Art no. 993, doi: 10.3390/land11070993.

[72] G. M. Foody, "Explaining the unsuitability of the kappa coefficient in the assessment and comparison of the accuracy of thematic maps obtained by image classification," *Remote Sensing of Environment,* vol. 239, p. 111630, 2020/03/15/ 2020, doi: https://doi.org/10.1016/j.rse.2019.111630.
[73] Y. Jia, "Object-based land cover classification with orthophoto and lidar data," ed, 2015.
[74] (2011). *Standards for reflectance*

spectral measurement of

temporal vegetation plots. [Online] Available: https://www.dcceew.gov.au/sites/default/files/documents/ssr195.pdf

Annex I

Nomenclatura_COSc.pdf

Appendix A

```
var roi = ee.FeatureCollection([ee.Feature(geometry)]);
var s2 = ee.ImageCollection("COPERNICUS/S2_SR_HARMONIZED");
var dem = ee.Image('USGS/SRTMGL1_003');
var bands = ['B2', 'B3', 'B4', 'B5', 'B6', 'B7', 'B8', 'B8A', 'B11', 'B12'];
var crs = 'EPSG:3763';

// Center the map on the reprojected roi
Map.centerObject(roi);

// A. Data preprocessing
// Step 1: Select image of cloud coverage below 10%
var Collection = s2.filterBounds(roi)
                   .filterDate('2022-07-06','2022-08-05')
                   .filterMetadata('CLOUDY_PIXEL_PERCENTAGE', 'less_than', 10);

print(Collection)

var image = ee.Image('COPERNICUS/S2_SR_HARMONIZED/20220802T112119_20220802T112118_T29TPE')
  .clip(roi);

print(image)
```

Figure A 1. Coding for filtering ROI, date, and cloud coverage.

```
// B. Spectral Indices Calculation
// 1. NDVI
// Create a function for NDVI
function addNDVI(band){
  var ndvi = band.normalizedDifference(['B8','B4']).rename('NDVI');
  var consistentBands = band.toFloat().addBands(ndvi.toFloat());
  return consistentBands;
}

// Apply NDVI to the cloud-masked images
var ndvi1 = addNDVI(cfImage1_3763).select('NDVI');
var ndvi2 = addNDVI(cfImage2_3763).select('NDVI');
var ndvi3 = addNDVI(cfImage3_3763).select('NDVI');


// Define a function to calculate DNBR
function calculateDNBR (preFireImage, postFireImage) {
  // Compute NBR for pre-fire image
  var preFireNBR = preFireImage.normalizedDifference(['B8A', 'B12']);

  // Compute NBR for post-fire image
  var postFireNBR = postFireImage.normalizedDifference(['B8A', 'B12']);

  // Compute DNBR
  var dnbr = preFireNBR.subtract(postFireNBR).multiply(1000);

  return dnbr;
}
```

Figure A 2. Coding for NDVI, NBR, and dNBR indices calculation.

```
// G. Spectral signature
var subset = image1.select(['B1', 'B2', 'B3', 'B4', 'B5', 'B6', 'B7', 'B8', 'B8A', 'B9', 'B11','B12']);

var samples = ee.FeatureCollection([
  Agriculture, Artificialized, Bareland, Forest,
  Shrub, Water
]);

// Sentinel-2 scale factor for reflectance conversion
var scaleFactor = 0.0001;

// Convert band values to reflectance
var subsetReflectance = subset.multiply(scaleFactor);

// Define wavelengths for each band
var wavelengths = [442.7, 492.4, 559.8, 664.6, 704.1, 740.5, 782.8, 832.8, 864.7, 945.1, 1613.7, 2202.4]

// Create scatter chart
var plotOptions ={
  title : 'Sentinel-2A Surface Reflectance Spectral',
  hAxis : {title:'Wavelength (nanometers)'},
  vAxis : {title: 'Reflectance'},
  lineWidth : 2,
  pointSize: 4,
  curveType: 'function',
  series:{
    0: {color:'FFFF00'},
    1: {color:'FF0000'},
    2: {color:'696969'},
    3: {color:'006400'},
    4: {color:'8B4513'},
    5: {color:'0000FF'},
  }
}

var chart = ui.Chart.image.regions(
  subsetReflectance, samples, ee.Reducer.mean(), 10, 'class', wavelengths)
  .setChartType('LineChart')
  .setOptions(plotOptions);

print(chart);
```

Figure A 3. Coding for spectral signature chart.

```
Imports (7 entries)
▸ var geometry: Polygon, 5 vertices
▸ var Agriculture: Feature 0 (GeometryCollection, 1 property)
▸ var Water: Feature 0 (MultiPolygon, 1 property)
▸ var Bareland: Feature 0 (GeometryCollection, 1 property)
▸ var Artificial: Feature 0 (GeometryCollection, 1 property)
▸ var Forest: Feature 0 (GeometryCollection, 1 property)
▸ var Shrub: Feature 0 (GeometryCollection, 1 property)
```

Figure A 4. Feature collection of the land cover classes in this research.

```
// Create cluster segment for OBIA
// Seeds
var seeds = ee.Algorithms.Image.Segmentation.seedGrid(20, 'hex');

// SNIC segmentation
var segment = ee.Algorithms.Image.Segmentation.SNIC({
  image: image,
  compactness: 0,
  seeds: seeds
}).reproject('EPSG:3763', null, 20);


// Image for classification
var imageObject = segment.select(['B.*']);
var bandsName = imageObject.bandNames();

var sample = ee.FeatureCollection([Agriculture, Artificial, Bareland,
  Forest, Shrub, Water]);


// #1: Object-Based Image Analysis (OBIA)
var trained_OBIA = imageObject.sampleRegions({
  collection: sample,
  scale: 20,
  properties: ['class']
});

// #2: Pixel-Based Image Analysis (PBIA)
var trained_PBIA = image.select(bands).sampleRegions({
  collection: sample,
  scale: 20,
  properties: ['class']
});
```

Figure A 5. Coding for SNIC segmentation, OBIA and PBIA land cover classification.

```
// Randomly split the samples into training and validation sets
// #1: OBIA
var sampleO = trained_OBIA.randomColumn('random');
var trainingSamples_O = sampleO.filter(ee.Filter.lt('random', 0.6));
var validationSamples_O = sampleO.filter(ee.Filter.gte('random', 0.6));

// #2: PBIA
var sampleP = trained_PBIA.randomColumn('random');
var trainingSamples_P = sampleP.filter(ee.Filter.lt('random', 0.6));
var validationSamples_P = sampleP.filter(ee.Filter.gte('random', 0.6));
```

Figure A 6. Coding for training and test dataset into a ratio of 60:40.

```
// E. Image classification using ML algorithm
// Classifier
// #1: Random Forest x OBIA
var classifierRF_O = ee.Classifier.smileRandomForest(30).train(trainingSamples_O, 'class', bandsName);
var LCORF = imageObject.classify(classifierRF_O);

// #2: Random Forest x PBIA
var classifierRF_P = ee.Classifier.smileRandomForest(30).train(trainingSamples_P, 'class', bands);
var classifiedRF_P = trainingSamples_P.classify(classifierRF_P);

// #3: SVM x OBIA
var classifierSVM_O = ee.Classifier.libsvm().train(trainingSamples_O, 'class', bandsName);
var LCOSVM = imageObject.classify(classifierSVM_O);

// #4: SVM x PBIA
var classifierSVM_P = ee.Classifier.libsvm().train(trainingSamples_P, 'class', bands);
var classifiedSVM_P = trainingSamples_P.classify(classifierSVM_P);

// Apply the trained RF classifier to the S2 imagery
var classifiedRFSummer23 = image.select(bands).classify(classifierRF_P);
var RFSummer23 = classifiedRFSummer23.reproject({
  crs: 'EPSG:3763',
  scale: 20
});

// Apply the trained SVM classifier to the S2 imagery
var classifiedSVMSummer23 = image.select(bands).classify(classifierSVM_P);
var SVMSummer23 = classifiedSVMSummer23.reproject({
  crs: 'EPSG:3763',
  scale: 20
});
```

Figure A 7. Coding to train RF and SVM classifier with OBIA and PBIA approaches.

```
// F. Calculation for Confusion Matrix
// Function to evaluate classifier and print confusion matrix, overall accuracy, and kappa coefficient
function evaluateClassifier(classifier, validationSamples, name) {
  var confusionMatrix = ee.ConfusionMatrix(validationSamples.classify(classifier)
    .errorMatrix({
      actual: 'class',
      predicted: 'classification'
    }));

  print('Confusion Matrix (' + name + ')', confusionMatrix);
  print('Precision (' + name + ')', confusionMatrix.consumersAccuracy());
  print('Recall (' + name + ')', confusionMatrix.producersAccuracy());
  print('Overall Accuracy (' + name + ')', confusionMatrix.accuracy().format('%.2f'));
  print('Kappa Coefficient (' + name + ')', confusionMatrix.kappa().format('%.2f'));
  print('F1 Score (' + name + ')', confusionMatrix.fscore(1));
}

// Example usage
evaluateClassifier(classifierRF_O, validationSamples_O, 'RF_O');
evaluateClassifier(classifierRF_P, validationSamples_P, 'RF_P');
evaluateClassifier(classifierSVM_O, validationSamples_O, 'SVM_O');
evaluateClassifier(classifierSVM_P, validationSamples_P, 'SVM_P');
```

Figure A 8. Coding for confusion matrix, precision, recall, OA, kappa coefficient, and F1 score calculation.

Appendix B

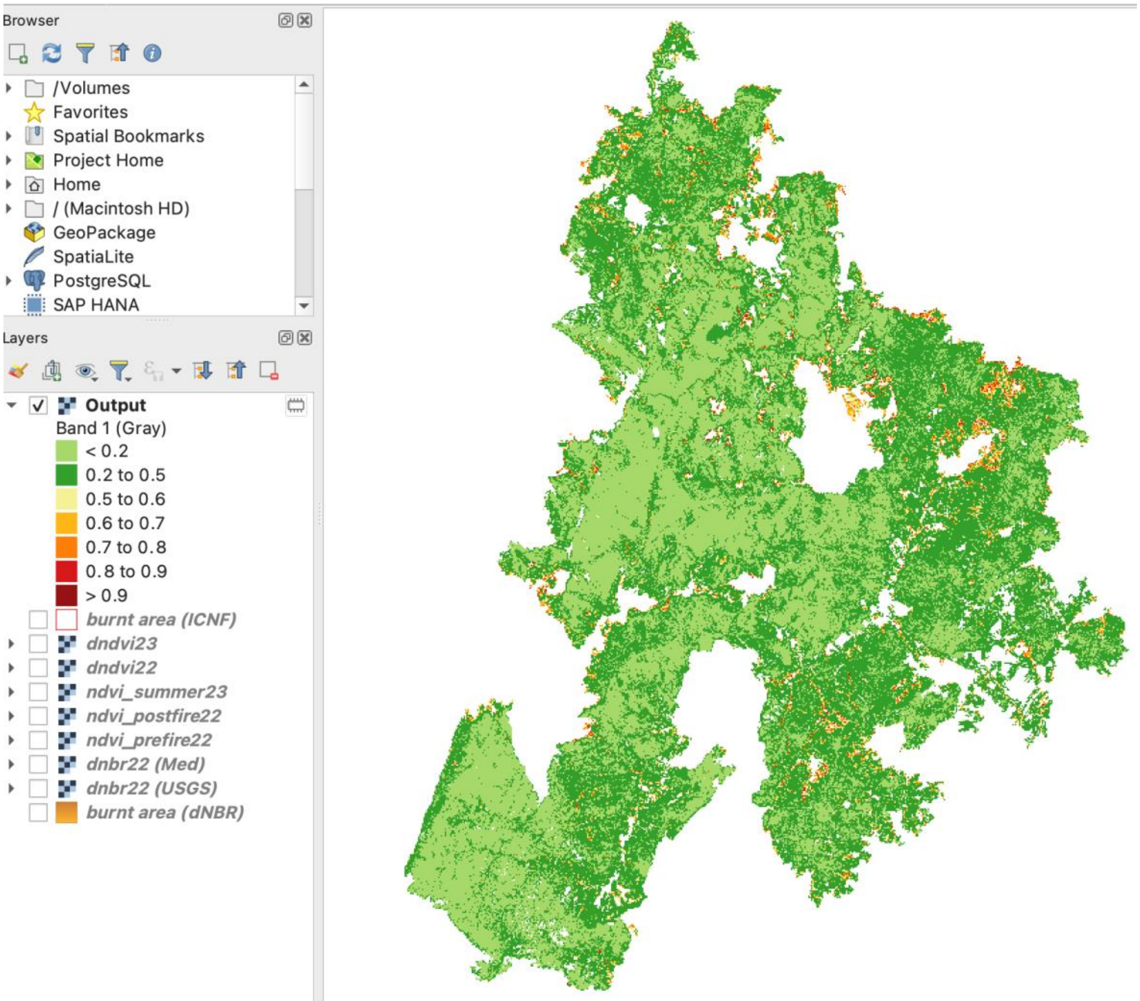

Figure B 1. NDVI value post-wildfire 2022.

Table B 1. Land size of the study area in different NDVI values post-wildfire 2022.

NDVI Value	< 0.2	0.2 - 0.5	0.5 - 0.6	0.6 - 0.7	0.7 - 0.8	0.8 - 0.9	> 0.9	Total
Number of Pixel (100m²)	1044359	1208460	80482	49107	29160	11697	597	2423862
%	43.09	49.86	3.32	2.03	1.20	0.48	0.02	100

Appendix C

Table C 1. Confusion Matrix of RF x PBIA model [pre-wildfire 2022].

RF x PBIA	0	1	2	3	4	5	**Precision**
0	897	2	20	143	53	0	0.8045
1	2	300	28	0	6	0	0.8929
2	8	17	1029	2	16	0	0.9599
3	39	0	0	2545	16	0	0.9788
4	105	12	73	81	595	0	0.6871
5	0	0	0	0	0	56	1
Recall	0.8535	0.9063	0.8949	0.9184	0.8673	1	

Table C 2. Confusion Matrix of SVM x OBIA model [pre-wildfire 2022].

SVM x OBIA	0	1	2	3	4	5	**Precision**
0	910	21	89	37	68	0	0.8089
1	33	298	0	0	11	0	0.8713
2	55	0	1022	0	62	0	0.8973
3	770	8	63	1631	131	0	0.6266
4	133	19	68	12	565	0	0.7089
5	0	0	0	0	0	72	1
Recall	0.4787	0.8613	0.8229	0.9708	0.675	1	

Table C 3. Confusion Matrix of SVM x PBIA model [pre-wildfire 2022].

SVM x PBIA	0	1	2	3	4	5	Precision
0	692	5	63	242	113	0	0.6206
1	12	309	12	0	3	0	0.9196
2	76	21	968	0	7	0	0.903
3	146	0	2	2407	45	0	0.9258
4	209	11	127	73	446	0	0.515
5	0	0	0	0	0	56	1
Recall	0.6097	0.8931	0.8259	0.8843	0.7264	1	

Table C 4. Confusion Matrix of RF x PBIA model [post-wildfire 2022].

RF x PBIA	0	1	2	3	4	5	Precision
0	1046	5	4	61	38	0	0.9064
1	2	222	2	0	0	0	0.9823
2	3	4	2601	0	0	0	0.9973
3	54	0	0	1006	11	0	0.9393
4	115	0	0	18	160	0	0.5461
5	0	0	0	0	0	54	1
Recall	0.8574	0.961	0.9977	0.9272	0.7656	1	

Table C 5. Confusion Matrix of SVM x OBIA model [post-wildfire 2022].

SVM x OBIA	0	1	2	3	4	5	Precision
0	1007	12	0	66	67	0	0.8741
1	5	192	0	0	34	0	0.8312
2	0	0	2586	0	0	0	1
3	105	2	6	893	14	0	0.8755
4	110	18	6	8	162	0	0.5329
5	0	0	0	0	0	49	1
Recall	0.8207	0.8571	0.9954	0.9235	0.5848	1	

Table C 6. Confusion Matrix of SVM x PBIA model [post-wildfire 2022].

SVM x PBIA	0	1	2	3	4	5	Precision
0	797	2	16	249	79	0	0.6973
1	11	207	6	0	0	0	0.9241
2	18	13	2554	0	0	0	0.988
3	185	0	0	860	11	0	0.8144
4	223	2	0	11	83	0	0.2602
5	0	0	0	0	0	53	1
Recall	0.6459	0.9241	0.9915	0.7679	0.4798	1	

Table C 7. Confusion Matrix of RF x PBIA model [summer 2023].

RF x PBIA	0	1	2	3	4	5	Precision
0	1107	0	10	78	58	0	0.8835
1	9	155	49	0	12	0	0.6889
2	7	8	2254	0	1	0	0.993
3	34	0	0	2302	2	0	0.9846
4	158	2	4	0	336	0	0.672
5	0	0	0	0	0	99	1
Recall	0.8418	0.9394	0.9728	0.9672	0.8215	1	

Table C 8. Confusion Matrix of SVM x OBIA model [summer 2023].

SVM x OBIA	0	1	2	3	4	5	Precision
0	1169	0	0	11	47	0	0.9527
1	0	185	0	1	20	0	0.8981
2	0	3	2298	0	0	0	0.9987
3	33	20	0	2223	8	0	0.9733
4	18	18	0	6	452	0	0.915
5	0	0	0	0	0	97	1
Recall	0.9582	0.8186	1	0.992	0.8577	1	

Table C 9. Confusion Matrix of SVM x PBIA model [summer 2023].

SVM x PBIA	0	1	2	3	4	5	Precision
0	996	0	33	106	148	0	0.7763
1	9	166	42	0	8	0	0.7378
2	27	10	2227	0	6	0	0.9811
3	196	23	0	2111	8	0	0.9029
4	162	2	17	8	311	0	0.622
5	0	0	0	0	0	99	1
Recall	0.7165	0.8259	0.9603	0.9488	0.6466	1	

Appendix D

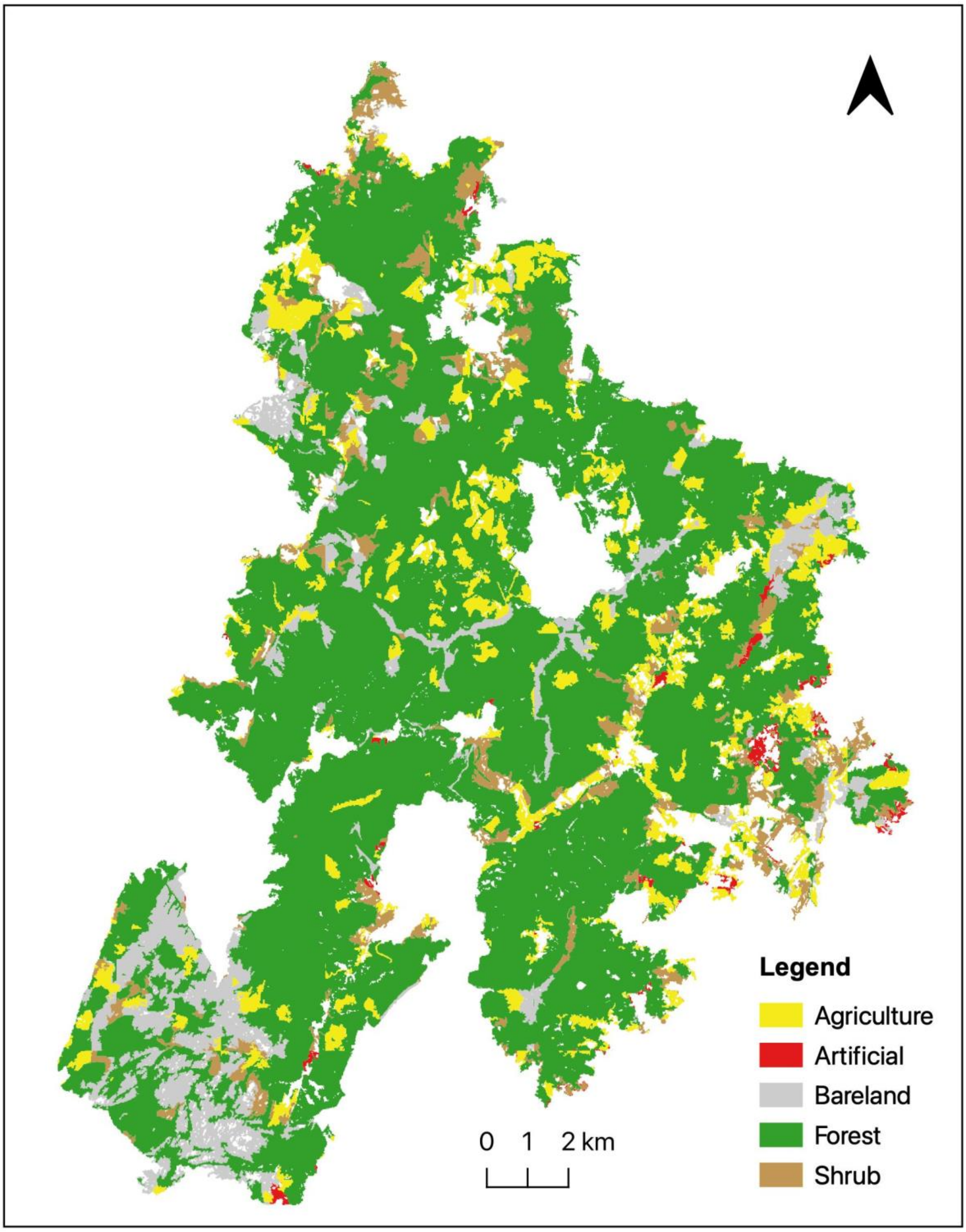

Figure D 1. RF_OBIA_S22.

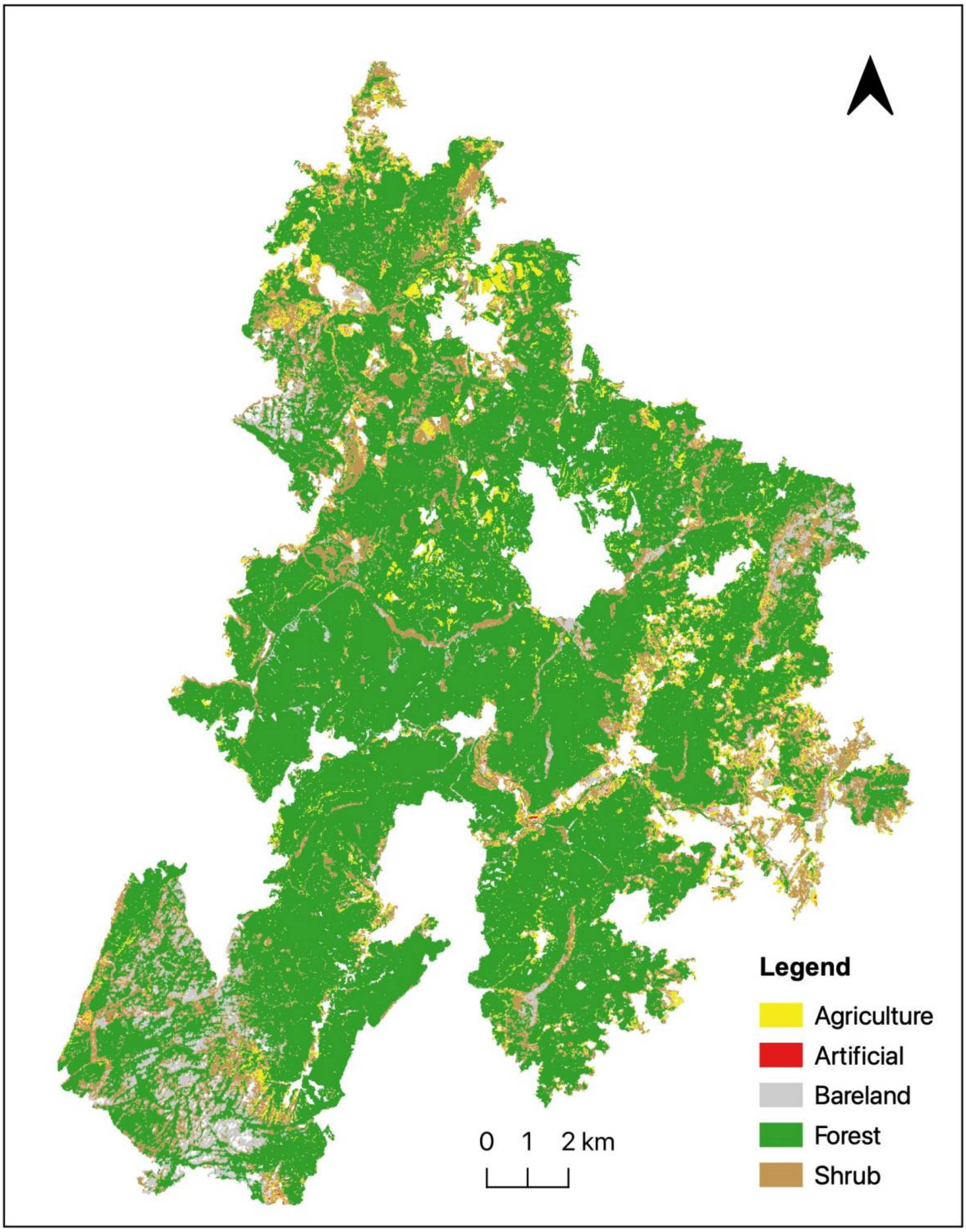

Figure D 2. RF_PBIA_S22.

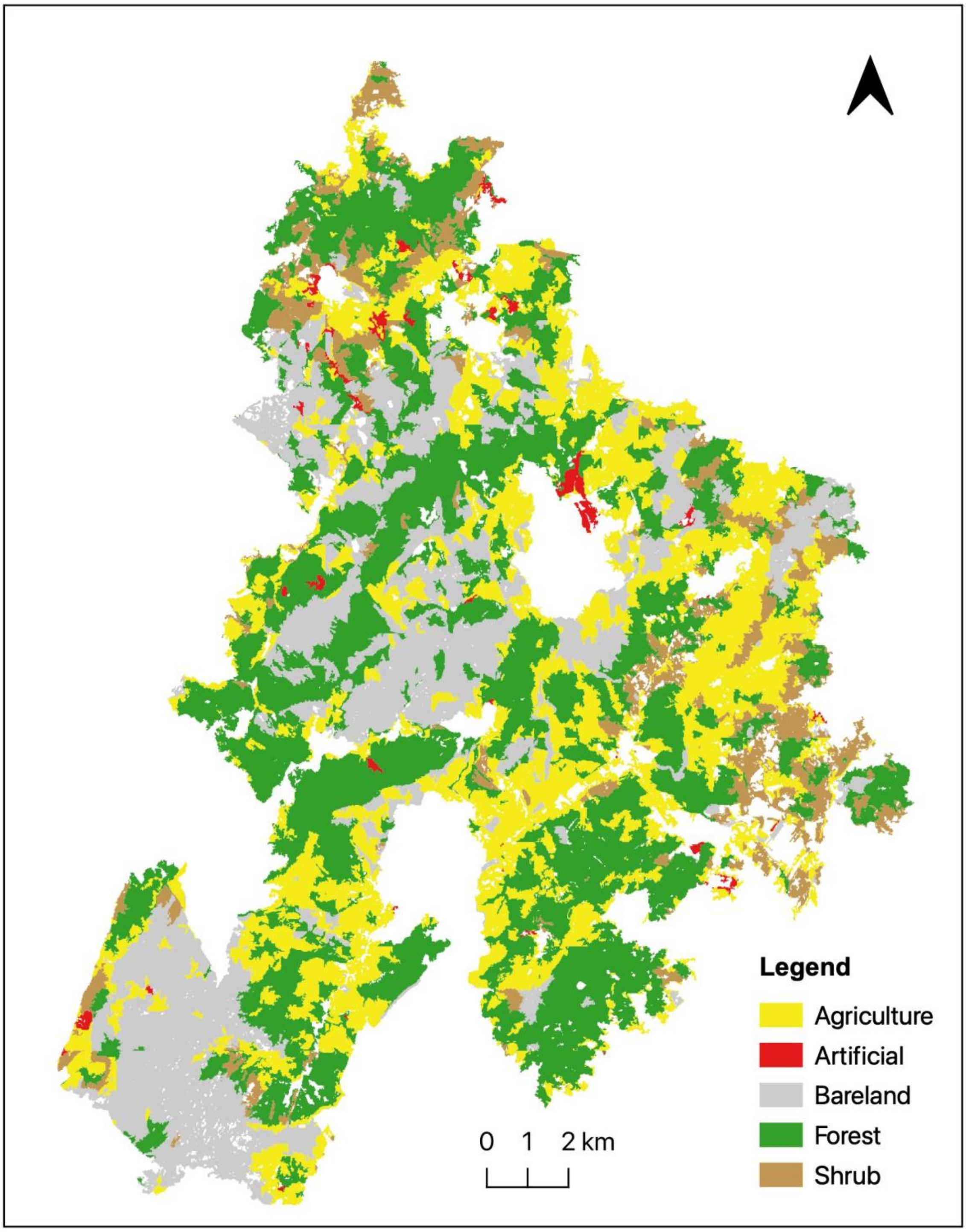

Figure D 3. SVM_OBIA_S22.

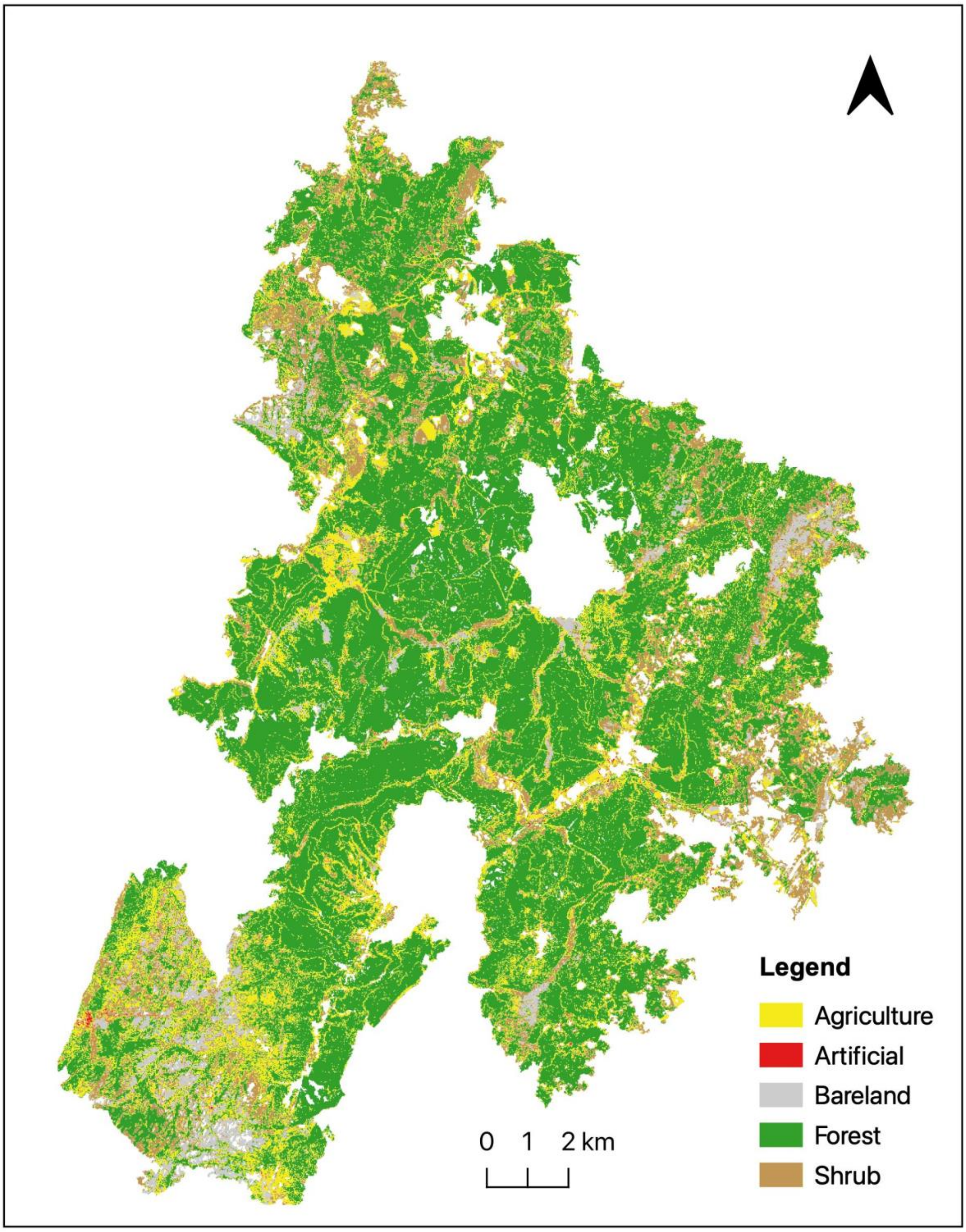

Figure D 4. SVM_PBIA_S22.

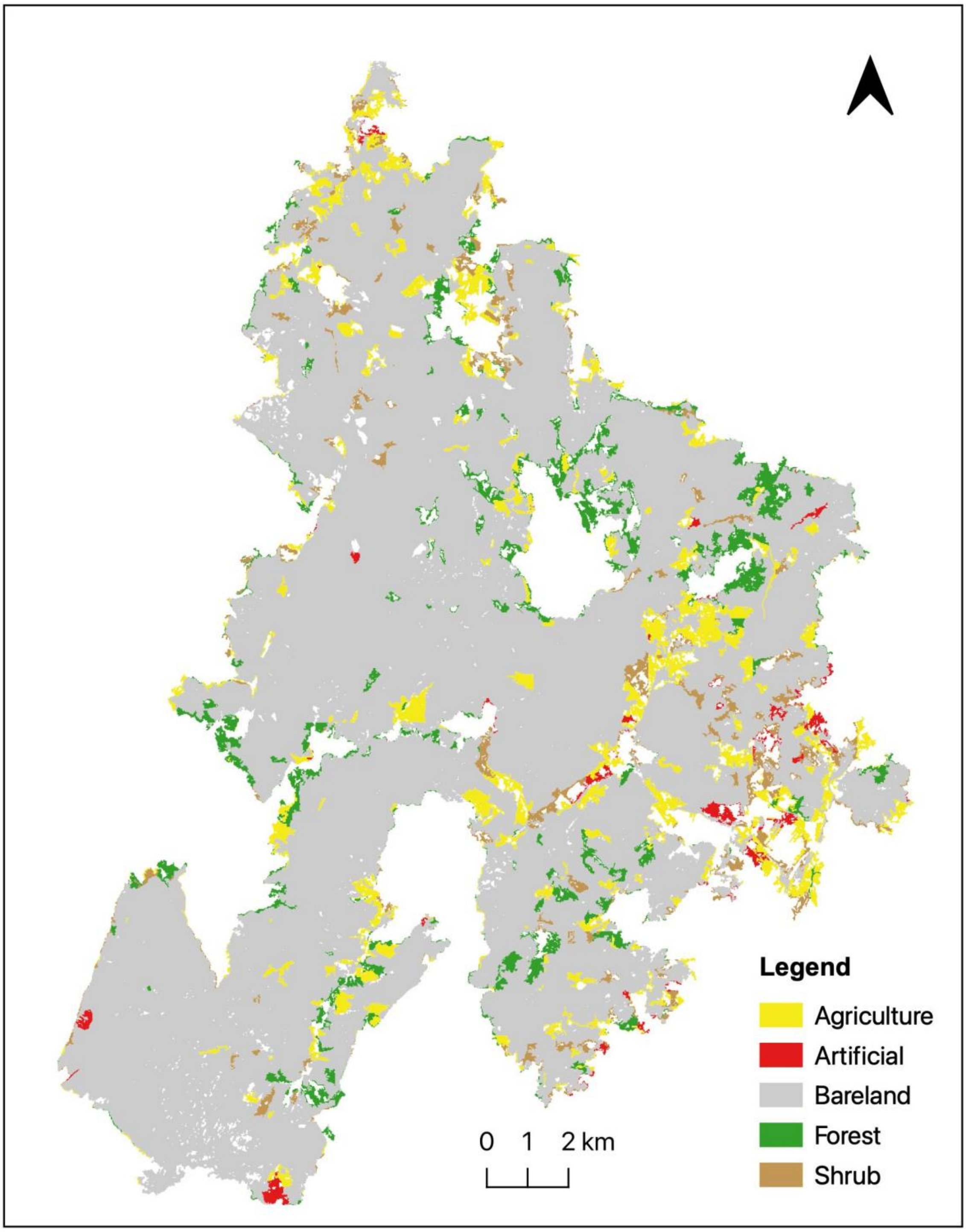

Figure D 5. RF_OBIA_F22.

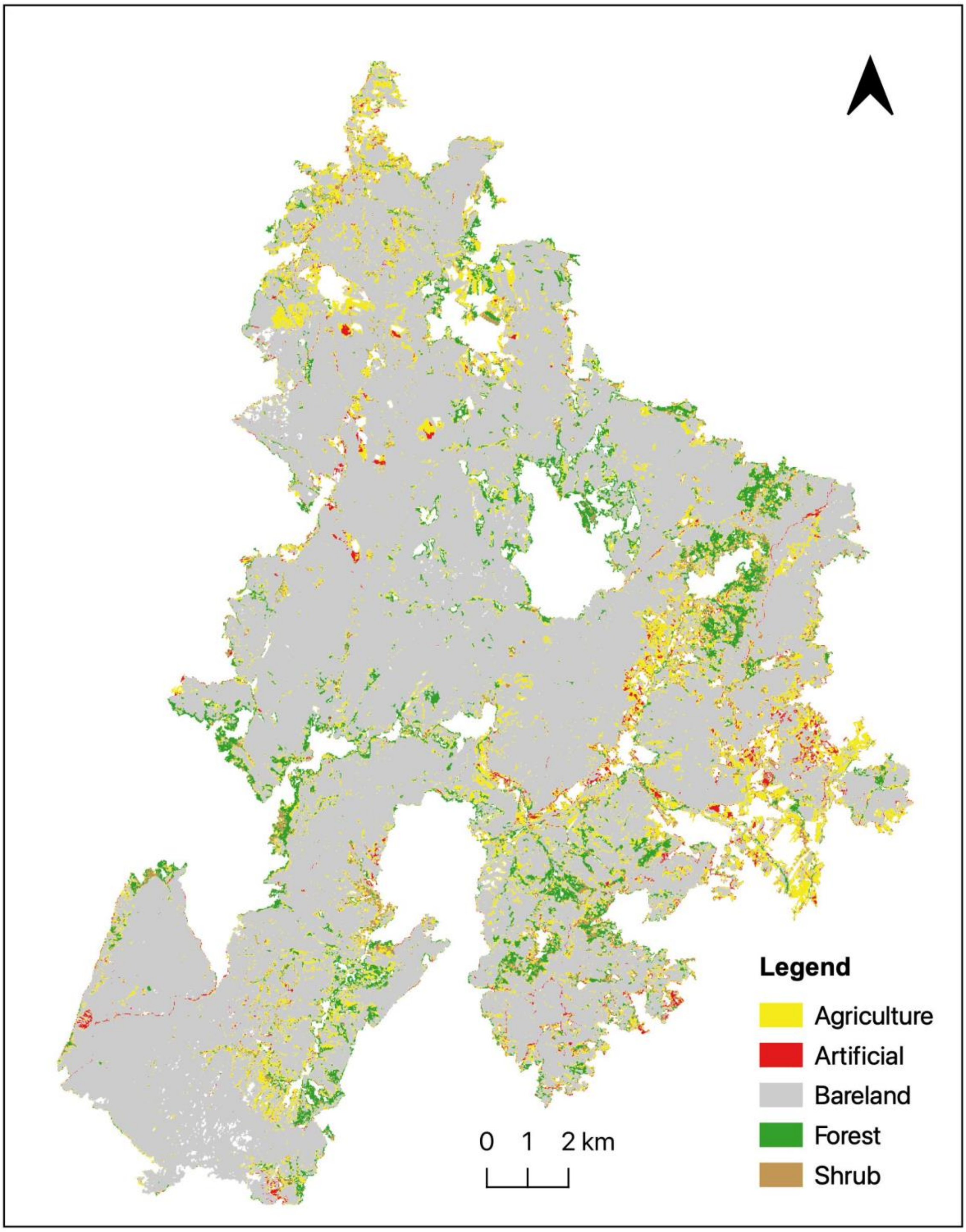

Figure D 6. RF_PBIA_F22.

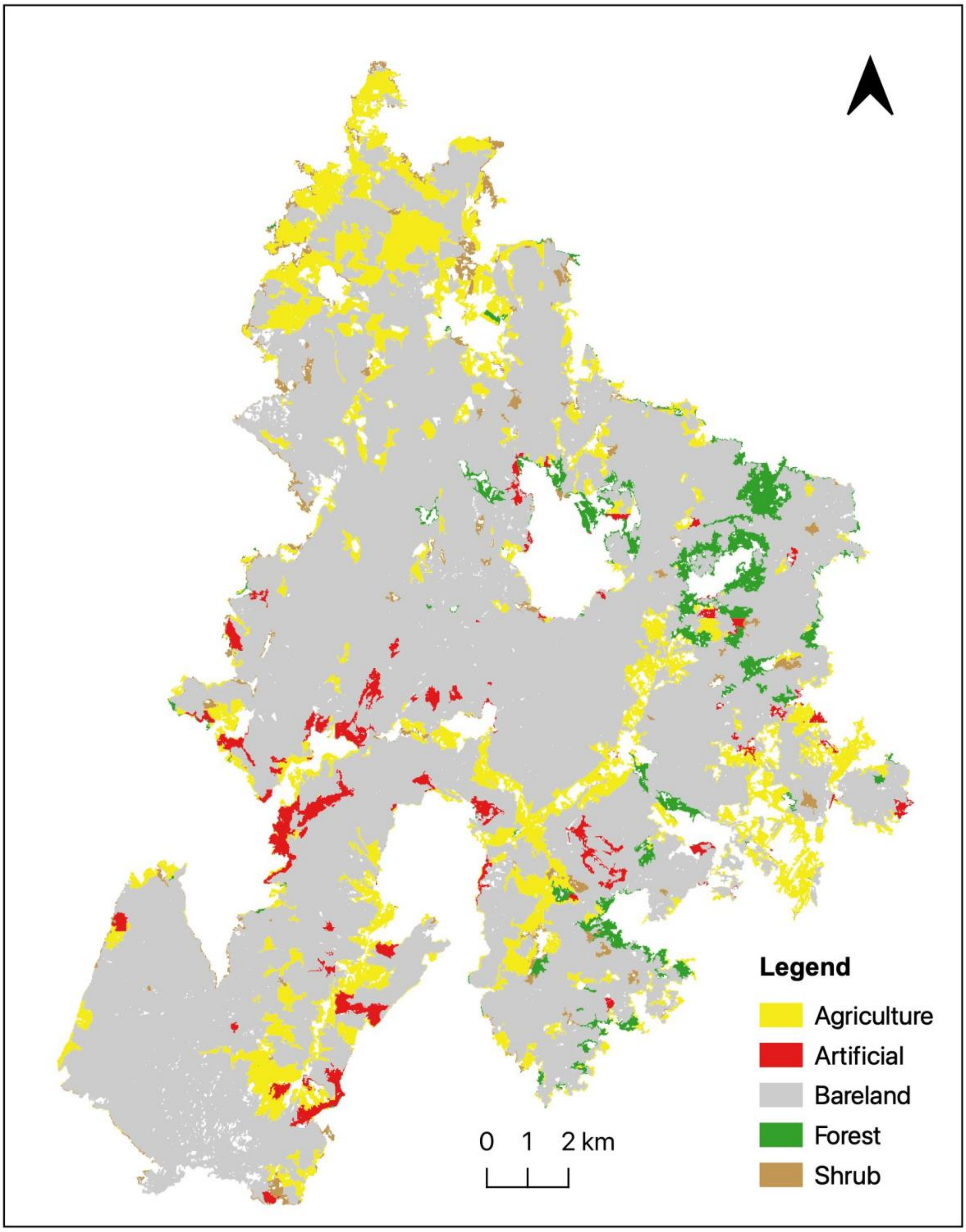

Figure D 7. SVM_OBIA_F22.

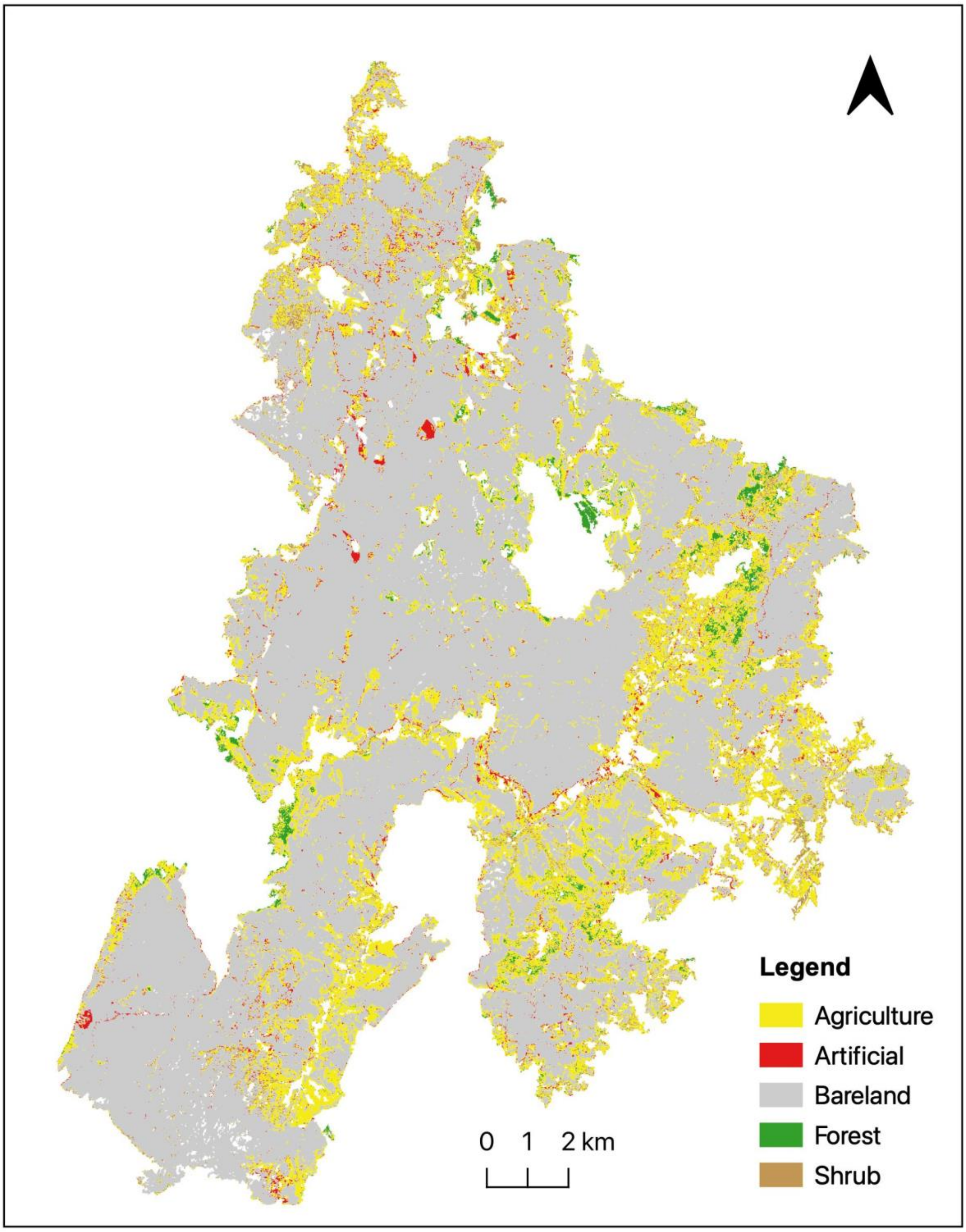

Figure D 8. SVM_PBIA_F22.

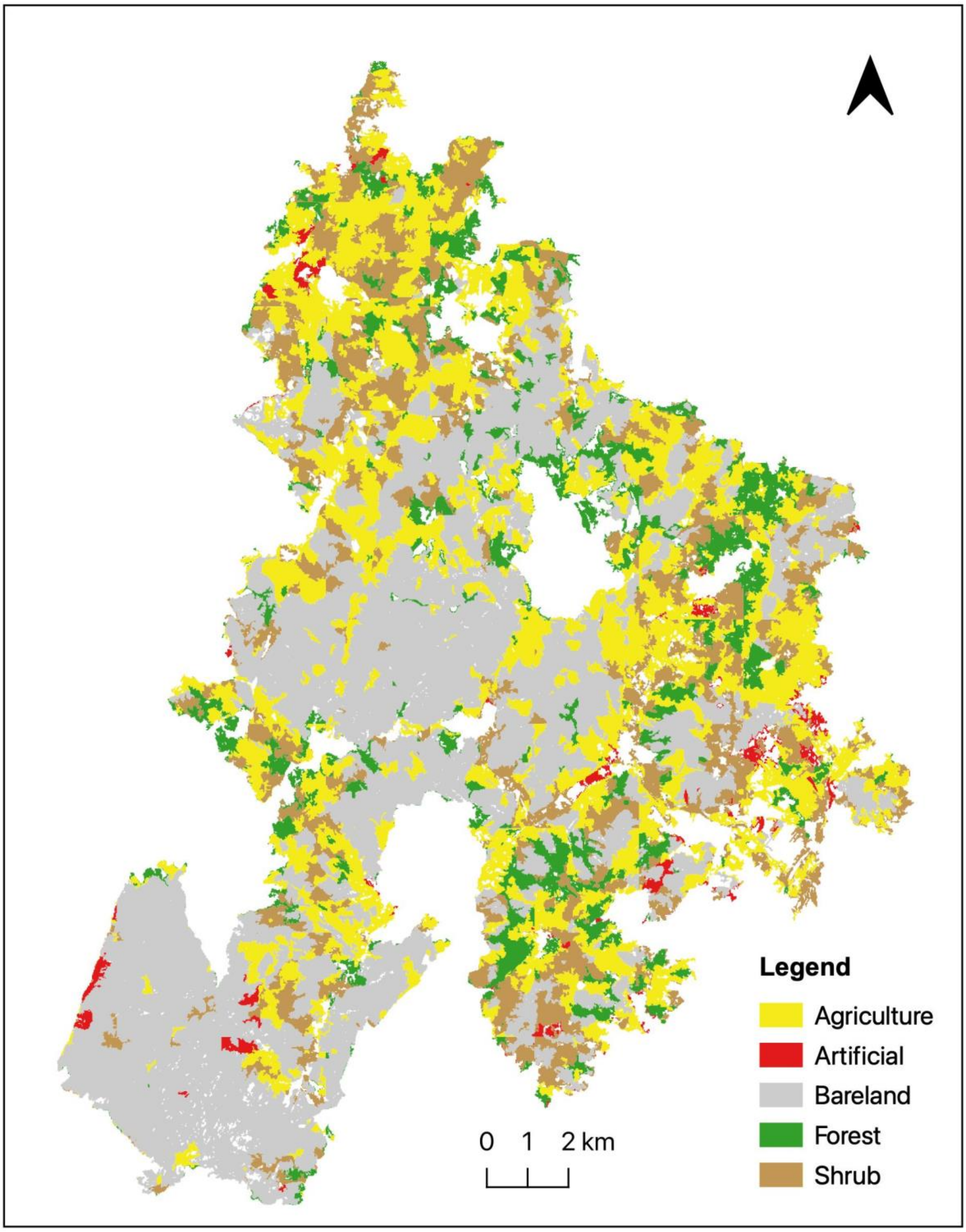

Figure D 9. RF_OBIA_S23.

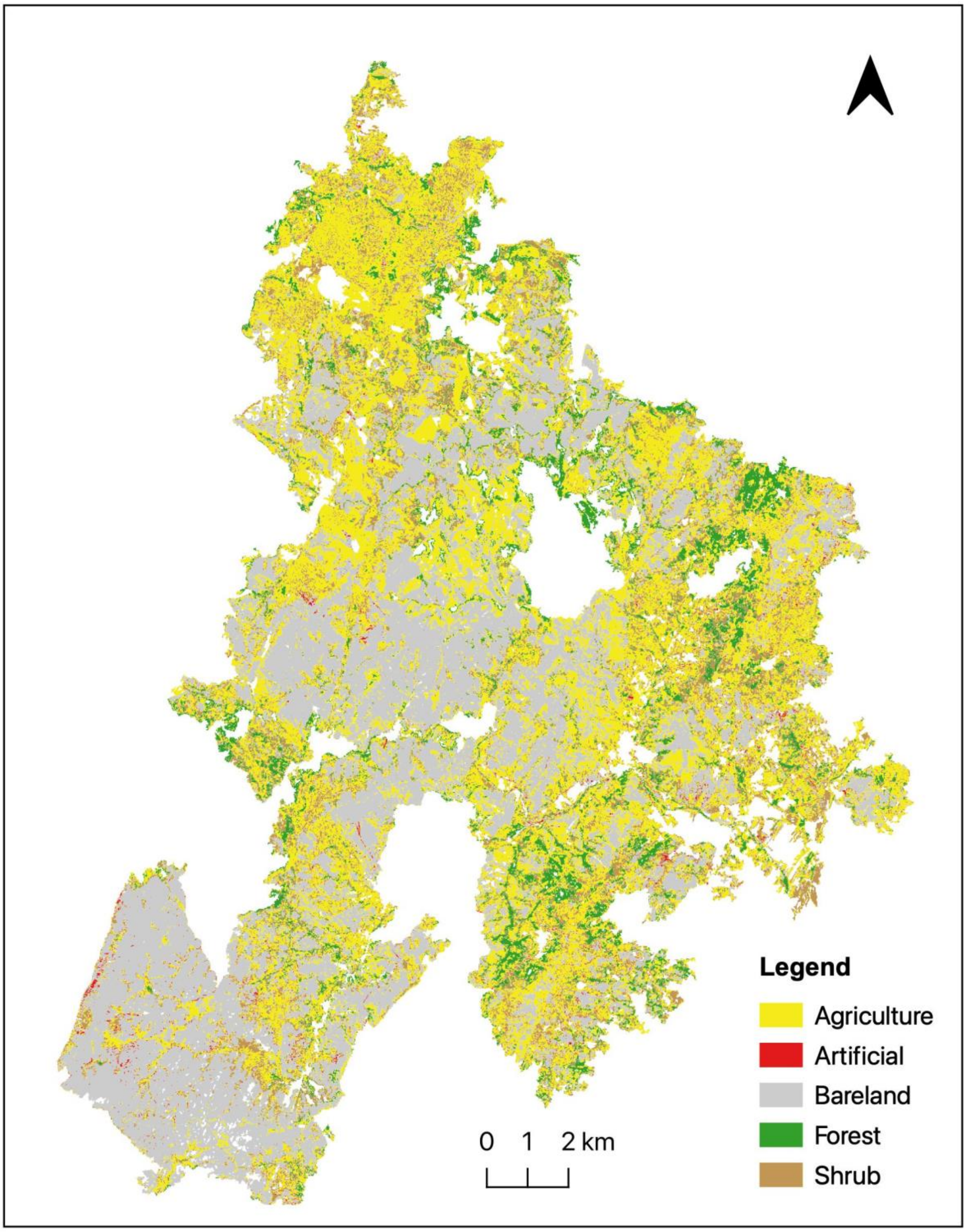

Figure D 10. RF_PBIA_S23.

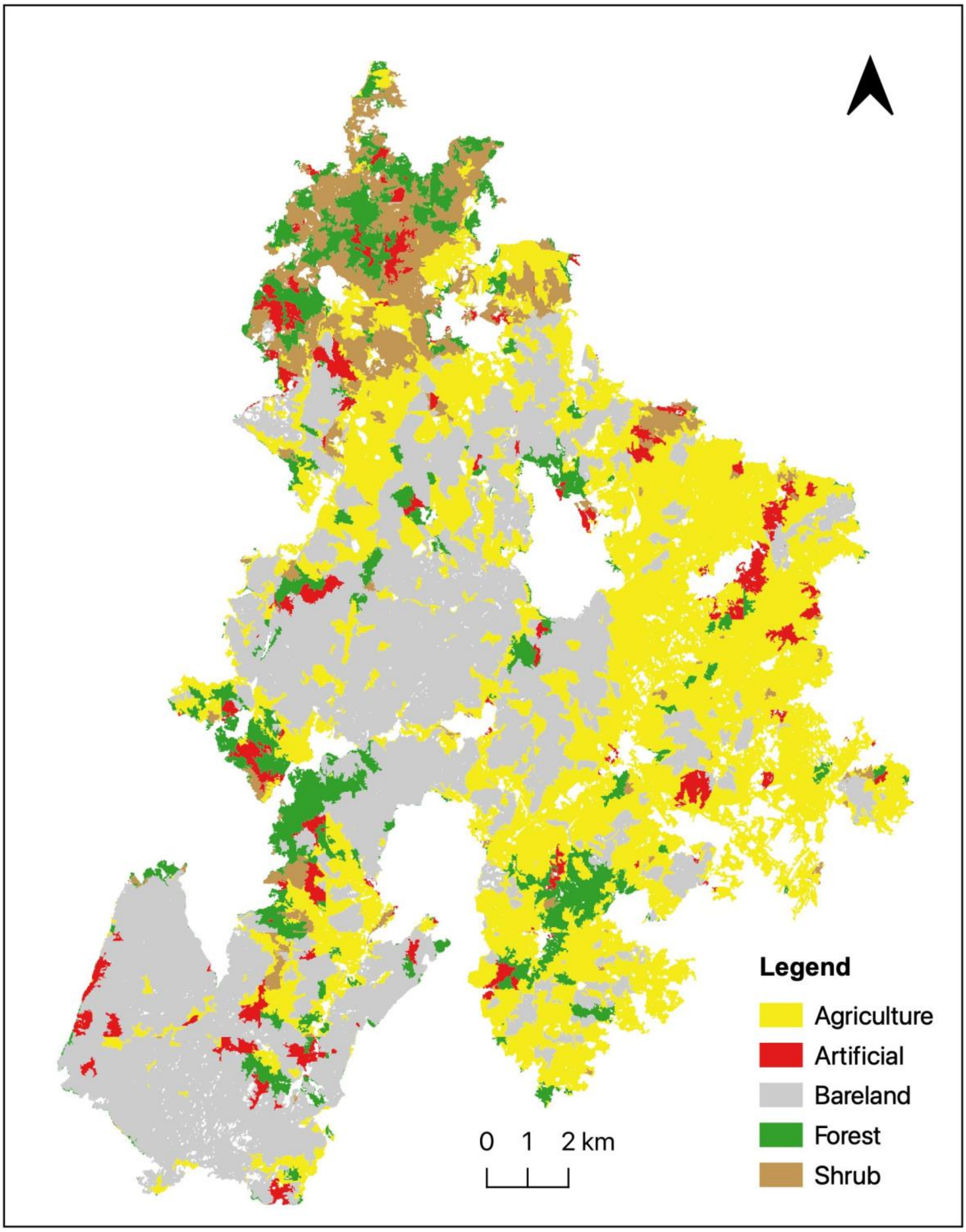

Figure D 11. SVM_OBIA_S23.

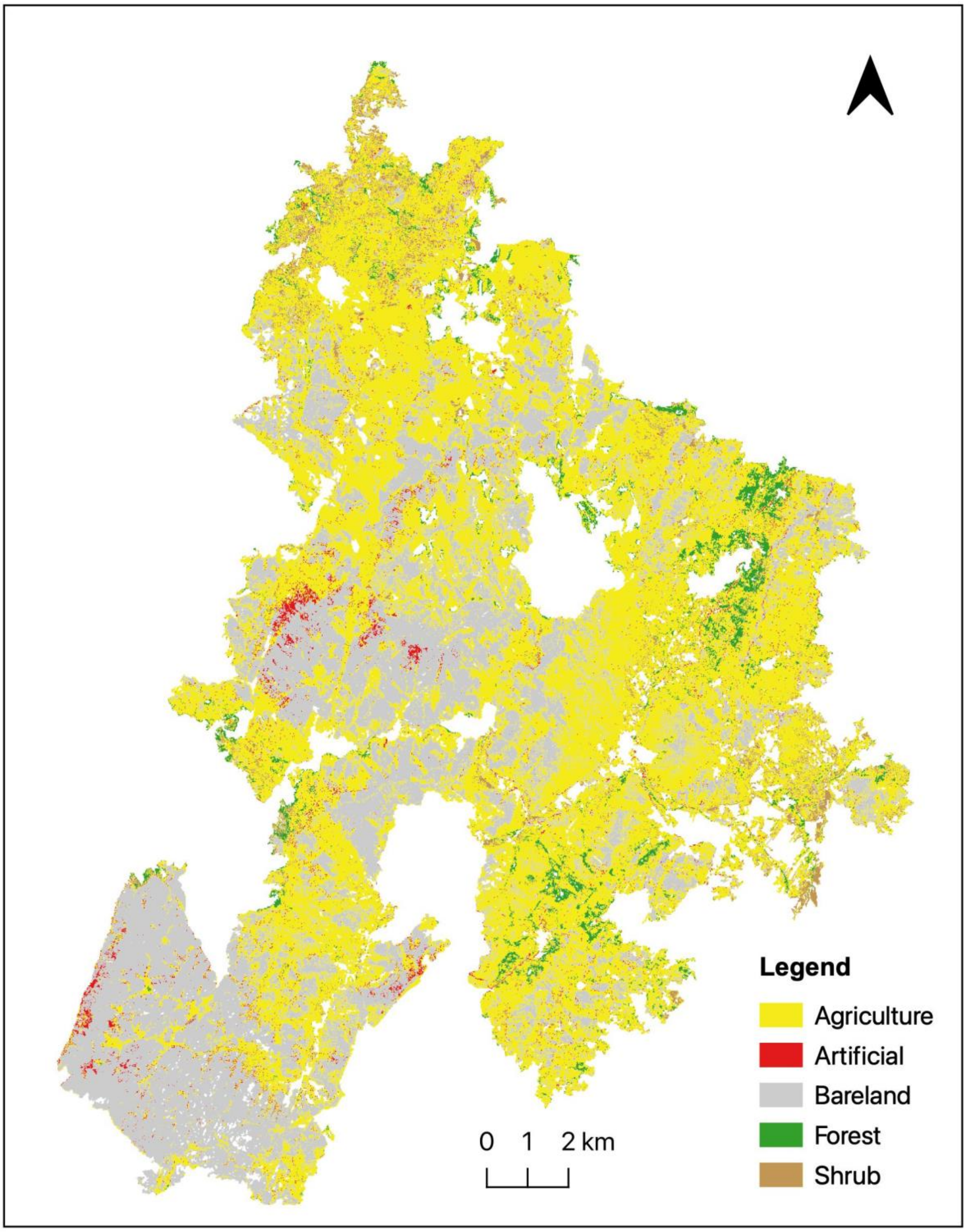

Figure D 12. SVM_PBIA_S23.